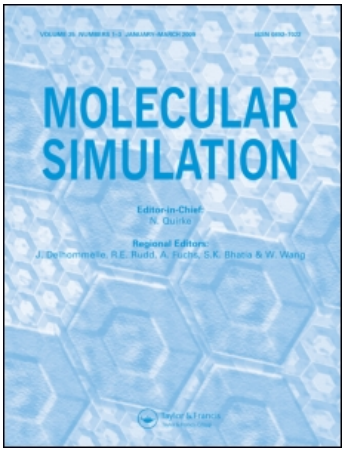

Molecular Simulation
Publication details, including instructions for authors and subscription information:
http://www.informaworld.com/smpp/title~content=t713644482

Atomistic modelling of adsorption and segregation at inorganic solid interfaces

Jeremy P. Allen[a]; Wojciech Greń[a]; Marco Molinari[b]; Corinne Arrouvel[a]; Filippo Maglia[b]; Stephen C. Parker[a]
[a] Department of Chemistry, University of Bath, Bath, UK [b] Department of Physical Chemistry, University of Pavia, Pavia, Italy

To cite this Article Allen, Jeremy P. , Greń, Wojciech , Molinari, Marco , Arrouvel, Corinne , Maglia, Filippo and Parker, Stephen C.(2009) 'Atomistic modelling of adsorption and segregation at inorganic solid interfaces', Molecular Simulation, 35: 7, 584 — 608
To link to this Article: DOI: 10.1080/08927020902774570
URL: http://dx.doi.org/10.1080/08927020902774570

Molecular Simulation
Vol. 35, No. 7, June 2009, 584–608

Taylor & Francis
Taylor & Francis Group

Atomistic modelling of adsorption and segregation at inorganic solid interfaces

Jeremy P. Allen[a], Wojciech Greń[a], Marco Molinari[b], Corinne Arrouvel[a], Filippo Maglia[b] and Stephen C. Parker[a]*

[a]*Department of Chemistry, University of Bath, Claverton Down, Bath BA2 7AY, UK;* [b]*Department of Physical Chemistry, University of Pavia, Viale Taramelli, 16, I-27100 Pavia, Italy*

(*Received 31 October 2008; final version received 25 January 2009*)

Recent work using atomistic simulations on a number of different oxide and mineral interfaces is described. Static simulation techniques have been applied to gadolinium doped ceria grain boundaries and show that there is marked variation in oxygen vacancy and dopant segregation with depth and orientation of a number of tilt boundaries. These methods have also been used to model the carbonation of magnesium and calcium hydroxide surfaces and predict that the calcium hydroxide is more reactive, particularly {1 0 1} and {1 0 2} surfaces. Another important interface studied is the solid–water interface and we report a number of recent molecular dynamics simulations which show how the water ordering is affected by structure and composition. These include showing that calcium oxide–water interfaces show a range of water ordering including the appearance of ice-like structures, and on carbonation the water structure is totally disrupted. Simulations on the water ordering at silica–water interfaces predict that {11.0} quartz surfaces are more hydrophobic than {10.0} leading in turn to a preference for organic adsorption on {11.0}, while preliminary results for a siliceous porous surface suggest that the water structure influences the transport properties at the surface, particularly by extremes of pH.

Keywords: energy minimisation; molecular dynamics; LTA; calcium hydroxide; calcium oxide; quartz; ceria

1. Introduction

Understanding adsorption and segregation processes at oxide and mineral interfaces is important as the modified structure and composition will impact on many properties such as the reactivity and transport. Computer modelling is an ideal technique to use for probing the effect of adsorption and segregation because it can evaluate the effect of these processes at the atomic level, helping to predict and guide experimental work. In this paper, we describe our recent progress in a number of current projects all focusing on modelling adsorption or segregation at three key mineral interfaces, namely the mineral–vacuum, mineral–water and mineral–mineral interfaces, using both static and dynamic simulation techniques.

We begin by showing how the static simulation methods can be used effectively for modelling segregation at interfaces. Initially, we will report on work characterising selected ceria grain boundaries, which are of key importance to work on solid oxide fuel cells. The static methods allow us to predict both the structure and stability of the boundaries as well as the effect of both oxygen vacancies and dopant species, which play an important role in controlling the oxygen transport in the material, allowing it to be used as an electrolyte. The second example is where we model the energetics of adsorption and mineral surface alteration in the presence of carbon dioxide, of importance to both carbon sequestration and the cement industry. The study will consider both the mode of adsorption, through the addition of a carbonate group as well as the energetics involved on the key surfaces of calcium and magnesium hydroxides. Additionally, studies of water adsorption allow us to compare the competitiveness of these two key species with regard to surface adsorption.

When considering minerals in a natural environment, the mineral–water interface is the next most logical interface to study, to increase the realism of the simulation. The mineral–water interface is important to study because it can play a large role in affecting the reactivity at real surfaces. The study of this interface can help elucidate not only the structure of the water but also the transport properties to and across the surface. We begin by again considering carbonate altered surfaces, initially evaluating the structuring of water at different CaO surface terminations and the effects that the surface adsorption of carbonate has. Then we detail our models of the structure of water above silica surfaces, considering both quartz and porous siliceous zeolite structures. We then show the extent to which we have increased the complexity by showing recent simulations of interacting pollutants with two quartz surfaces and the effect of pH on the structuring of water and diffusivity above zeolite surfaces.

*Corresponding author. Email: s.c.parker@bath.ac.uk

ISSN 0892-7022 print/ISSN 1029-0435 online

DOI: 10.1080/08927020902774570
http://www.informaworld.com

We will begin by discussing the use of both static and dynamical simulation techniques that are required for these studies prior to the analysis of the results.

2. Methodology

The work in this study uses classical potential modelling exclusively and is based on the Born model of ionic solids [1]. This assumes that the interactions existing within a system can be considered as long-range electrostatic [2–4] and short-range forces, where the short-range forces are represented by parameterised analytical functions which are fitted to either experimental or *ab-initio* data. These models also include ionic polarisability. We use the shell model, introduced by Dick and Overhauser [5], which represents the polarisable ion as a core, containing the mass of the ion, which is connected to a shell by a spring.

In this work we employed both static and dynamic lattice simulation techniques. The static lattice energy minimisations used the METADISE [6] code, which was originally designed to model dislocations, interfaces and surfaces. METADISE uses a two-region approach, considering the crystal as being comprised of two blocks, each consisting of two regions, I and II, which are periodic in two dimensions. Those atoms near the interface are incorporated into region I while region II represents the rest of the crystal. The inclusion of region II ensures that all the ions in region I experience the forces associated with the rest of the crystal and that the energies are fully converged. Region I ions are allowed to relax to their mechanical equilibrium, whereas region II ions are kept fixed at their bulk equilibrium positions. To achieve energy convergence, the number of ions in region I and II have to be sufficiently large.

The surface energy, γ, of a crystal face is defined as the excess in energy of a surface simulation, U_S, over the energy of a bulk system, U_B, containing the same number of atoms per unit area, S. The surface energy becomes:

$$\gamma = \frac{U_S - U_B}{S}. \quad (1)$$

The dynamical simulations in this work are carried out exclusively using the DL_POLY [7] molecular dynamics code. Calculations are primarily run using the NVT ensemble. In all simulations, the temperature is kept constant at 300 K using the Nosé–Hoover thermostat [8,9], with the Verlet-Leapfrog algorithm [10] used to generate the trajectories. The motion of the shells was treated using the adiabatic approach described by Mitchell and Fincham [11], where the shells are assigned a small, fictional mass of 0.2 au. Thus, the timestep used is 0.2 fs, allowing the simulations to prevent the shells moving an unrealistic distance between steps. For all simulations, a real space cut off of 8 Å was used.

3. Static simulation applied to segregation and adsorption processes

3.1 Ceria grain boundaries

Over the last few years, fluorite-structured ceramic materials have received a lot of attention [12,13] due to their unique combination of physical, chemical and mechanical properties [14]. The interest in these functional oxide materials has been driven by their important technological applications, particularly as electrolyte materials in solid state electrochemical devices, such as solid oxide fuel cells (SOFC). However, the widespread use of these devices has been hampered by a number of technological problems, mainly due to the need to operate at high temperatures. The use of solid electrolytes based on cerium dioxide (ceria) allows for a reduction of the SOFC working temperature [12–17] compared to stabilised zirconia. Unlike zirconia, ceria does not need to be doped to stabilise the cubic fluorite structure. It has also been suggested that further improvement can be obtained through the use of electrolyte materials in a nanoparticle form [18,19]. These materials, however, are characterised by a large number of grain boundaries, whose role in defining the defect equilibria and electrical conductivity in ionic materials is still poorly understood [20–22].

In order to further understand the role of grain boundaries, their structure and the extent to which defects segregate or accumulate at the boundaries need to be studied. It is well known that many of the properties of the polycrystalline materials depend on the structure and composition of the interfaces between the grains. In fluorite-structured ceramic oxides, the boundaries represent the main contribution to the resistance to transport. This results in the diffusivity being much lower than in the single crystals [23]. It is therefore important to understand the effects that occur at the interfaces and how these can affect the macroscopic properties. The aim of this work is to investigate both the distribution of point defects as well as the defect stability in proximity of a grain boundary in gadolinium-doped ceria. This material has been selected as doping with gadolinium induces the highest ionic conductivity of all doped ceria materials, possibly due to a lower lattice strain, as shown by lattice parameter measurements [24]. There are a range of previous studies of fluorite structured gadolinium-doped ceria surfaces and interfaces. The initial studies include the consideration of defect cluster formation by Minervini et al. [24] and oxygen migration by Balducci et al. [25]. In addition, both Sayle et al. [26] and Nolan et al. [27] have modelled ceria surfaces, whereas Fisher et al. [28] has used molecular dynamics to study stabilised zirconia interfaces. Recent work has also considered ceria nanoparticles [29] and nanotubes [30]. However, a deeper understanding of the structures and the effects of defects segregation on the ionic conductivity is still required, particularly

in nanometric materials where the boundary conductivity is expected to play a dominant role in the macroscopic properties.

The potential model used to simulate ceria is that of Sayle et al. [27], as modified by Balducci et al. [31] and discussed by Martin et al. [30,32]. The interactions between ceria and gadolinium ions are taken from the work of Minervini et al. [24].

3.1.1 Mirror twin grain boundary structure and segregation

The grain boundary structures were constructed from the most stable surfaces, which were modelled first to find the lowest energy structures. The modelled surfaces consist of the (3 1 0), (3 1 1) and (3 3 1) surfaces. The (3 1 0) surface was selected for study as it was the first twin grain boundary modelled for a fluorite-structured oxide, that of yttrium-stabilised zirconia by Fisher et al., therefore allowing a comparison of the results. The remaining two surfaces were chosen to complement the work on the (3 1 0) surface. Another advantage of choosing these surfaces is that they are relatively quick to model, while higher index surfaces may be more computationally expensive to scan, therefore allowing us to refine our methods of simulation prior to considering more complex boundaries. The lowest energy cuts of these surfaces were found to have surface energies of 4.24, 3.41 and 2.23 J/m^2 for the (3 1 0), (3 1 1) and (3 3 1) surfaces, respectively. Additionally, all three surfaces are oxygen-terminated and this termination is maintained on minimisation. Figure 1 details the structures of both the unrelaxed and relaxed structures for the three materials.

A marked surface reconstruction is seen on the (3 1 0) surface, Figure 1(a), where the relaxation of ions occurs to a depth of approximately 13 Å. This reconstruction is reflected by changes in both the oxygen and cerium sublattices. The cerium atoms at the surface move off their lattice positions, which results in significant surface oxygen atom rearrangement around the cerium atoms, giving the (3 1 0) surface a faceted-like appearance. Minimisation of the (3 1 1) surface, however, only shows an oxygen sublattice rearrangement, to a depth of 4 Å, with the cerium sublattice remaining fixed with no distortion.

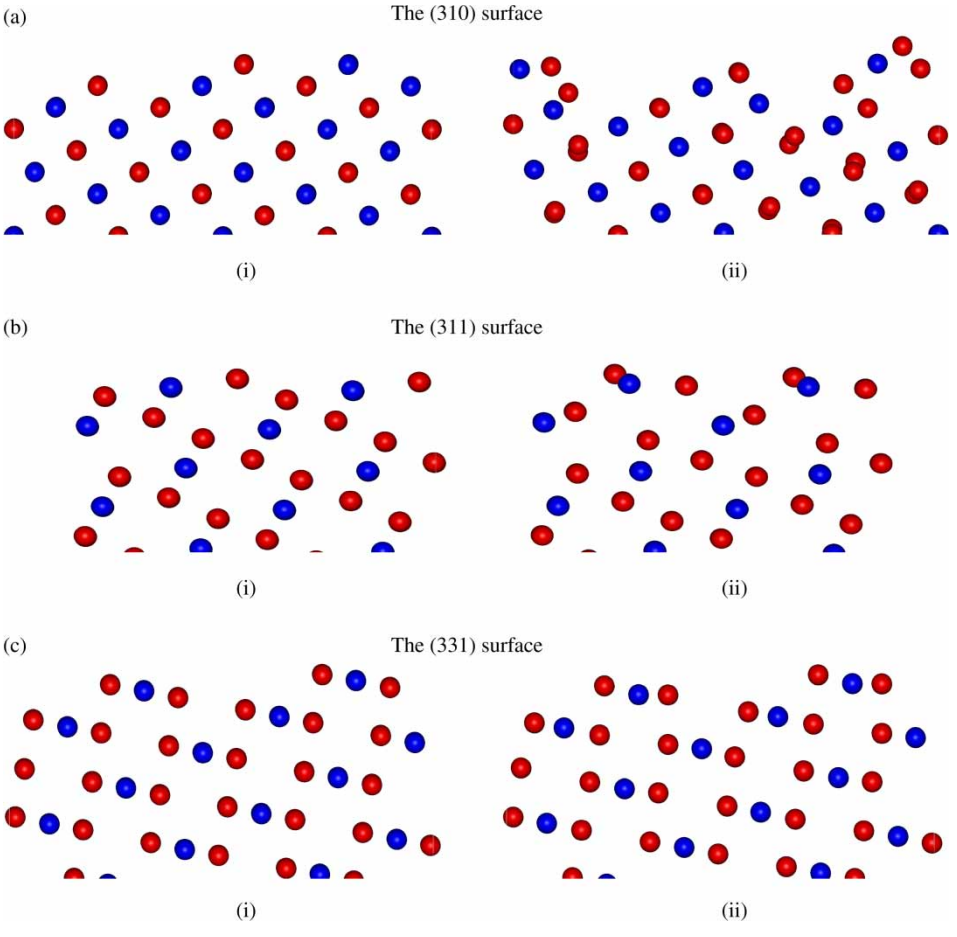

Figure 1. The average positions of ions at (i) unrelaxed and (ii) the corresponding relaxed surface terminations of the (a) (3 1 0), (b) (3 1 1) and (c) (3 3 1) CeO_2 surfaces. Note: Oxygen atoms are coloured red whereas cerium atoms are represented by blue.

The most stable of the three surfaces is the (3 3 1) though, which also represents the most ordered surface of the three under study.

These surfaces were used to construct the grain boundaries. Blocks of ceria were generated with surface and bulk regions for each termination. The grain boundaries were then generated for each of the three surface terminations by mirroring the unrelaxed surfaces, with a gap of 2 Å introduced between the two surfaces. One of the crystal blocks was then held fixed and the second scanned across the surface to find the most stable configuration. The block was moved in steps of 0.2 Å in the two dimensions in the plane parallel to the interface, thus allowing the whole interface to be scanned. At each point in the scan, the structure was allowed to relax until the energy converged, which included allowing a rigid displacement of the more distant atoms normal to the interface plane. This allows the movable block to approach the fixed block when the interactions between the two are favourable, whilst moving away when repulsion dominates. The relaxed energy sampled at each position can be monitored using a two-dimensional grid representing the interface plane. The grid points themselves represent the minima in surface energy and therefore were assumed to be the more stable grain boundary configurations. However, it is important to note that this method of grain boundary construction introduces two major simplifications that are worth considering. The first is that only mirror images of the same surface are joined to form a grain boundary, whereas it is entirely feasible that two different surfaces, or even surface terminations of the same index, may result in a more stable configuration than those modelled. Second, surface faceting has not been explicitly taken into account, which could also affect the stability of the grain boundary, possibly resulting in a more stable interface.

Table 1. The formation, E_f, and cleavage, E_c, energies for the (3 1 0), (3 1 1) and (3 3 1) twin grain boundaries of ceria.

Twin grain boundary	E_f (J/m^2)	E_c (J/m^2)
(3 1 0)	3.37	5.81
(3 1 1)	1.70	5.13
(3 3 1)	2.42	2.06

The formation energy, E_f, and the cleavage energy, E_c, were calculated for each pure twin grain boundary by using Equations (2) and (3), respectively,

$$E_f = E_{gb} - E_b, \tag{2}$$

$$E_c = 2 \times (E_s - (E_{gb}/2)), \tag{3}$$

where E_{gb}, E_b and E_s are the grain boundary, bulk and surface energies, respectively. The cleavage energy is defined as the energy that is necessary to separate two grains. The formation and cleavage energies of the three twin grain boundaries are summarised in Table 1, with the structures shown in Figure 2.

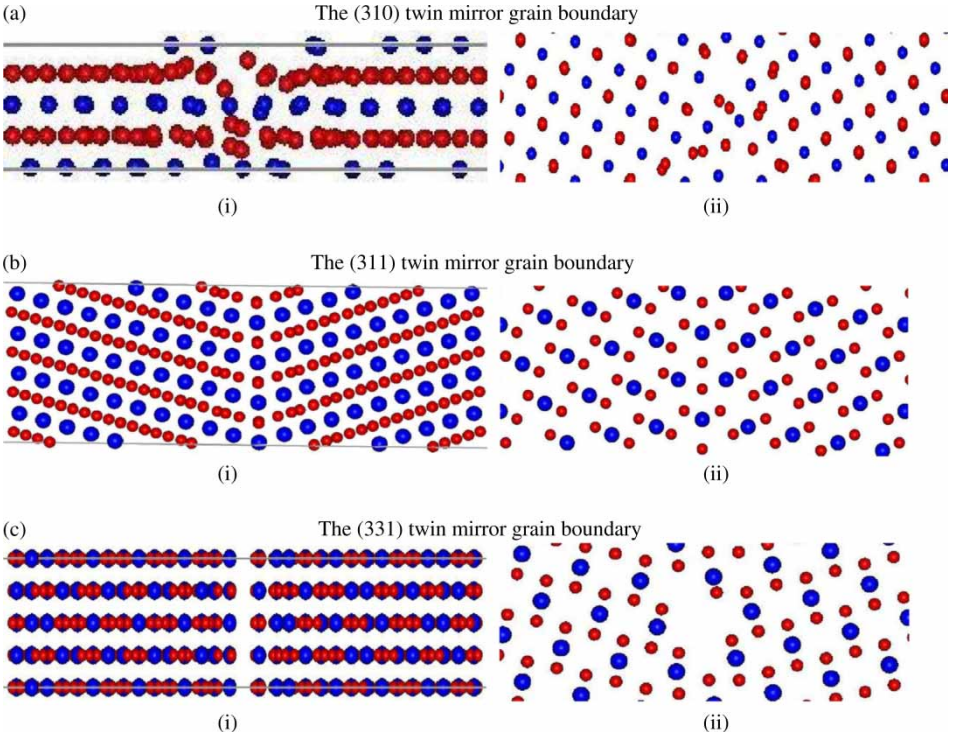

Figure 2. The average positions of ions at the (a) (3 1 0), (b) (3 1 1) and (c) (3 3 1) twin grain boundaries of ceria, viewed along the (i) *x*- and (ii) *y*-axes.

The energies of formation show the (3 1 1) twin grain boundary to have the lowest value, followed by the (3 3 1) and (3 1 0) grain boundaries. In contrast, the cleavage energies do not follow the same trend, with the (3 1 0) having the largest energy and the (3 3 1) having the lowest. However, to consider the stability of the grain boundary, both formation and cleavage energies need to be analysed together. The (3 1 0) twin boundary is the least stable, despite the cleavage energy, suggesting that a deeper rearrangement could hamper the splitting of the structure into two individual grains. The (3 1 1) symmetrical twin grain boundary shows the most stable structure with a formation energy of 1.70 J/m^2, with the minimisation leading to a marked match between the mirroring surfaces. The interpenetrating oxygen and cerium frameworks join the two blocks strongly together making their cleavage difficult. Table 1 shows that the formation of the (3 3 1) twin boundary is favourable but the resulting structure could break down easily along the grain boundary plane. The structures of the three grain boundaries show that there are specific regions along the interfaces which show a significant amount of cation and anion ordering. The (3 1 0) symmetrical tilt boundary width is approximately twice as large as the other two modelled surfaces, with a size of 20 Å. Whereas the (3 1 1) grain boundary has the smallest width of 6 Å, compared to 10 Å for the (3 3 1). The (3 1 0) boundary, unlike the others, has a large amount of disorder in both the oxygen and cerium frameworks, which is the most likely cause of the grain boundary instability.

The segregation of both gadolinium ions and an oxygen vacancy were then modelled on the three grain boundaries, through incorporation of these defects into one of the blocks forming the interface. The energy of incorporation of a dopant ion or defect into the interface can be directly compared to its energy of incorporation into the infinite bulk crystal, with the resultant energy representing an important component of the driving force for the dopant or defect to migrate from the bulk to the interface. Furthermore, interfaces have a finite thickness and hence the resultant energy or segregation energy, $\Delta H_{\mathrm{seg},z}$, will depend on distance, z away from the interface and can be calculated using (4)

$$\Delta H_{\mathrm{seg},z} = \Delta H^{\mathrm{interface}}_{\mathrm{dopants},z} - \Delta H^{\mathrm{bulk}}_{\mathrm{dopants}} = \left(H^{\mathrm{interface}}_{\mathrm{doped},z} - H^{\mathrm{interface}}_{\mathrm{undoped}}\right) - H_{V_O^{\bullet\bullet}} - 2H_{\mathrm{Gd}'_{\mathrm{Ce}}}, \quad (4)$$

where $\Delta H^{\mathrm{bulk}}_{\mathrm{dopants}}$ and $\Delta H^{\mathrm{interface}}_{\mathrm{dopants},z}$ are the energies of the incorporation of a dopant on a certain site i in the bulk and at a distance z from the interface, respectively. The incorporation of dopants at the interface can also be expressed as a function of the lattice energies of the doped, $H^{\mathrm{interface}}_{\mathrm{doped},z}$ and undoped, $H^{\mathrm{interface}}_{\mathrm{undoped}}$, structure. Similarly, the $\Delta H^{\mathrm{bulk}}_{\mathrm{dopants}}$ term can be replaced by the substitutional energies of the dopant on a regular bulk site at infinite separation. The enthalpies of segregation have been calculated for each site in the region I of the crystal as function of the distance from the interface, z. $\Delta H_{\mathrm{seg},0}$ is negative if the defect prefers energetically to reside at the interface, and as the value of the enthalpy of segregation is defined as the energy of incorporation relative to the bulk, it will converge to zero as z increases.

The segregation of gadolinium substitutional and oxygen vacancy defects was investigated using the following scheme. The segregation of an oxygen vacancy in a gadolinium-doped ceria grain boundary region initially involved placing two gadolinium atoms at the interface, added to compensate the charge. The gadolinium atoms were sited with a distance of separation large enough so that the atoms would be unable to interact with each other. The oxygen atoms were then removed sequentially from all possible sites in region I of the crystal. Gadolinium segregation was studied by the introduction of a single gadolinium and oxygen vacancy at different starting locations at the interface and the position of the second gadolinium was then varied. This resulted in the interface being singly positively charged and a single negative defect was replaced in order to maintain electroneutrality.

Region I of the block obviously contains a large number of sites to trial for gadolinium insertion. However, it is computationally inefficient to sample the placement of this dopant at all sites to find the most stable configurations. Therefore, METADISE was used to find the most likely sites for gadolinium incorporation. Initially, the total energies were calculated for all cerium and oxygen sites in region I. The regular sites to be replaced at the surface were then chosen as a result of their site energies. The site energy is dominated by the Madelung energy and hence there is an energetic preference for the lower charged Gd^{3+} ions to reside at the lower Madelung energy sites. The sites far from the interface have a fluorite-like bulk structure, whereas those at the interface have more complex coordination shells. This results in the site energies near the interface being different to the average bulk value.

The enthalpies of segregation of an oxygen vacancy from the bulk to the (3 1 1) and (3 3 1) twin mirrors are calculated to be approximately −4.2 and −2.8 eV, respectively. The enthalpies of segregation as a function of the distance from the interface, z, for the (3 1 1) and (3 3 1) twin mirrors boundaries are given in Table 2. The oxygen vacancy segregation enthalpy for the (3 1 1) grain boundary converges to zero at 13 Å distance from the boundary, with the (3 3 1) boundary converging to zero at a similar distance of 14 Å. As can be seen in Table 2, between 2 and 8 Å from the interface, the value of the segregation energy varies between −1.7 and −3.1 eV for

Table 2. The enthalpies of segregation for an oxygen vacancy as a function of distance, z, from the boundary interface for the (3 1 1) and (3 3 1) twin mirror Gd-doped ceria grain boundaries.

Grain boundary	Distance from the interface, z (Å)	$\Delta H_{seg,z}$ (eV)
(3 1 1) Twin	0.4	−2.2 to −4.2
	1.7	−3.1 to −3.8
	4.1	−2.6 to −2.7
	6.6	−1.7 to −1.9
	9.0	−1.2
	11.5	−0.6
	13.1	−0.1
(3 3 1) Twin	0.5	−2.8
	1.9	−1.6 to −2.8
	4.3	−1.3 to −2.1
	6.2	−1.2 to −1.8
	8.0	−1.1 to −1.3
	10.5	−0.7
	12.5	−0.3
	13.8	−0.1

the (3 1 1) boundary and −1.1 and −2.8 eV for the (3 3 1) boundary, suggesting that, in this region, the segregation of the oxygen vacancies is affected by the positions of the other defects which is likely to impact significantly on transport properties. The (3 1 0) twin mirror, not shown here, shows a distinctly different behaviour to the other two interfaces. The segregation enthalpy is, for the (3 1 0), considerably more affected than for the other two boundaries by the position of the replaced site, with respect to the positions of the other two defects in the boundary, even at much larger distances from the interface. The difference in the segregation enthalpy for different sites varies between −4.7 and −2.6 eV at the boundary and this variation is maintained deep into the bulk region. This large variation in site energies is also likely to reduce the ion mobility still further at this interface as the ions would have to negotiate large changes in site energies. The large spread of values for the enthalpy of segregation is likely due to the large depth of relaxation calculated for this interface, as shown previously by Figure 2(a).

The results of the gadolinium segregation also show that the starting location of the defects at the boundary has an influence on the results. For each boundary up to six starting configurations of defects at the interface were chosen. Table 3 gives the enthalpies of segregation for the two extreme configurations. The different starting configurations for the (3 1 1) twin boundary have minimum enthalpies of segregation between, approximately, −4.6 and −3.6 eV at a distance of 2.0 Å from the interface. This behaviour is also seen for the (3 1 0) twin mirror, with the segregation enthalpies at the interface for two different starting configurations of approximately −4.1 and −2.3 eV, with these minima occurring at a

Table 3. The enthalpies of segregation for a gadolinium ion as a function of distance, z, from the boundary interface at two different starting configurations of the (3 1 0), (3 1 1) and (3 3 1) twin mirror Gd-doped ceria grain boundaries.

Grain boundary	Distance from the interface, z (Å)	$\Delta H_{seg,z}$ for configuration I (eV)	$\Delta H_{seg,z}$ for configuration II (eV)
(3 1 0) Twin	0.7	−2.5	−3.5
	5.0	−2.3	−3.3 to −4.1
	10.0	−1.9	−2.9
	15.0	−1.3	−2.3
	20.0	−0.6	−1.6
	25.0	−0.1	−1.1
	30.0	NA	−0.4
(3 1 1) Twin	0.3	−2.0 to −2.6	−3.5 to −4.4
	2.0	−3.0 to −3.6	−4.2 to −4.6
	3.7	−2.4 to −2.8	−3.8 to −4.2
	7.0	−2.2 to −2.6	−3.9
	8.6	−2.2 to −2.4	−3.8
	10.3	−2.2	−3.6
	12.0	−2.0	−3.5
	13.5	−1.9	−3.4
	15.2	−1.6	−3.0
(3 3 1) Twin	0.2	−1.9 to −2.1	−2.8 to −3.2
	2.7	−1.2 to −2.0	−1.8 to −2.4
	4.0	−1.5 to −1.7 (−2.6)	−2.3 to −2.6 (−3.0)
	6.5	−1.4 to −1.9	−2.1 to −2.8
	9.0	−1.3 to −1.8	−2.0 to −2.4
	11.5	−1.2 to −1.5	−2.0 to −2.2
	14.0	−1.1 to −1.3	−1.8 to −2.0
	16.5	−0.9	−1.7

Values in parenthesis for (3 3 1) twin mirror grain boundary indicate lower energies seen for different starting configurations.

distance of 5.0 Å from the interface. The (3 3 1) twin boundary, however, has the most energetically favourable sites of −3.2 and −2.1 eV at the interface.

In summary, the atomistic calculations on gadolinium-doped ceria have considered the reconstruction of the three high Miller index surfaces as well as the grain boundary structure and segregation behaviour. The (3 3 1) surface was found to have the lowest surface energy, followed by the (3 1 1) and the (3 1 0), with the relaxed morphology of the (3 1 0) surface clearly showing a significant rearrangement of both the oxygen and cerium frameworks. The reconstruction for the other two surfaces, however, appeared to only involve the oxygen framework. For the twin grain boundaries, the order of increasing interfacial energy was different to that seen for surface stability. The (3 1 0) twin boundary still had the highest formation energy and the (3 1 1) twin grain boundary showed the lowest. However, the formation energies are not the only factors governing the stability of the grain boundaries. The interaction of the adjoining surfaces has to be taken into account, with the (3 1 0) twin boundary having the highest cleavage energy, followed by the (3 1 1) boundary, which has the most ordered structure at the interface. Overall, the balance between the formation energy and the difficulty of separating the two blocks suggest that the (3 1 1) twin boundary is the most stable of the three studied.

The segregation behaviour of the majority defects was also considered, with both the addition of gadolinium on cerium regular sites and the oxygen vacancy taken into account. The results show that the gadolinium enthalpies of segregation converge to zero more slowly than for oxygen vacancy segregation. This suggests the presence of a larger number of available cerium regular sites, which can accommodate trivalent dopant ions. From the initial results of this study, it is apparent that there is an intrinsic excess of both oxygen vacancies and gadolinium at the grain boundary. The segregation behaviour of the defects is clearly affected by both the structure of the twin boundary and the positions of the defects at the interface. Gadolinium segregates to the boundary due to the larger number of cerium regular sites which can easily accommodate the dopant ion, therefore a compensating oxygen vacancy excess is expected. The actual level of gadolinium segregation also depends on the amount of doping; suggesting further work is needed to clarify this effect. It would also be useful to study the possible imbalance of the oppositely charged defects in the boundary region, with particular attention to how it affects the segregation. Additionally, the level of segregation is also dependent upon the grain boundary configuration, therefore, it is also important to study twist grain boundaries to obtain representative behaviour.

The use of static lattice simulations can not only be applied to considering different structures of grain boundaries and large numbers of defect concentrations allowing segregation studies to be completed. Another area which can be effectively considered is the adsorption processes at surfaces. This method of scanning different configurations allows not only the effect of surface coverage to be assessed but also the rapid identification of those with the lowest adsorption energy. The next section will detail the work we have conducted to assess carbonate adsorption of different surfaces of calcium and magnesium hydroxide.

3.2 Carbonate adsorption on calcium and magnesium hydroxide surfaces

The interaction of water with surfaces is widely modelled due to the abundance of water in the environment. However, the interaction with other abundant gases is not as routinely studied. One such environmentally and technologically important process is the adsorption of carbon dioxide. The interaction of CO_2 with surfaces is particularly important with current concerns pointing towards the amount of anthropogenic carbon both in the atmosphere as well as being produced by industry. One potential method to help reduce this is through the process of carbon sequestration, where carbon dioxide is reacted with minerals to form the solid carbonate material which can then be suitably disposed in a more environmentally efficient manner.

Of the various systems available for use, the most promising appear to magnesium and calcium-rich materials due to their natural abundance and their availability in readily minable deposits. The first hypothetical mineral carbonation scheme was proposed by Seifritz [33], based on the natural weathering reaction of magnesium and calcium silicate minerals. This was then applied to magnesium hydroxide by Béarat [34], using gas-phase reactions at high CO_2 pressures. The aim of this was to gain a better understanding of the mechanisms of carbonation of materials containing hydroxide lamella, for example brucite ($Mg(OH)_2$) and serpentines (hydroxysilicates). Results indicated that the dehydroxylation of the material generally preceded the carbonation as a distinct yet interrelated process.

The consideration of hydroxide materials is also of importance due to the hydroxylation that occurs on many surfaces when in contact with water. For example, the chemisorption of water has been studied on magnesium and calcium oxide [35] and calcium carbonate [36] surfaces, showing it to be a favourable process. The carbonation of hydroxide minerals has also been considered using computational modelling, for example, Churakov et al. [37] considered the carbonation of brucite and the formation of the subsequent magnesium carbonate layer. Their study also concluded that the dehydroxylation of the surfaces will precede carbonation, although the carbonation process itself can also induce further dehydroxylation.

The aim of this work is to consider the initial stages of carbonation of magnesium and calcium hydroxides,

allowing for a direct comparison, through the addition of carbonate ions to a range of low index surfaces. In addition, the adsorption of water has also been considered to allow a comparison of the energetics of the two processes to be made, as well as analysis of the competition between the two species.

3.2.1 *Calculating surface free energies*

The adsorption of carbon dioxide onto the metal hydroxide surfaces is modelled as a post-reacted surface, through the adsorption of a carbonate group. To allow the free energy of the surface to be evaluated, through the calculation of the configurational entropy, the carbonation of the surface was modelled in two different ways (Figure 3). The first approach (Figure 3(a)) models the insertion of a carbonate *into* the surface, via the replacement of a surface hydroxide with a carbonate, and subsequent removal of a further hydroxide to keep the surface charge neutral. The second approach adds a carbonate *above* a surface by placement of a carbonate, in a bidentate manner, above a surface metal atom, followed by the removal of two surface hydroxides to balance the surface charge (Figure 3(b)). All combinations of removing two hydroxides from the surface were trialled, with carbonate alignment being modelled in both the *x*- and *y*-directions. Hydrated surfaces were generated by adding a water molecule 1.7 Å above a metal atom, with the hydrogen atoms pointing away form the surface. Overall, this gave rise to a total of 4464 individual static lattice energy minimisation calculations. Carbonated surface energies can be calculated directly from the 'pure' and 'modified' surface energies. The surface energy, γ, for a given configuration is given by (5)

$$\gamma = \frac{1}{S}[E_S - E_B] - \frac{1}{S} n_{CO_3^{2-}} E_{corr}\left(CO_3^{2-}\right), \qquad (5)$$

where S is the surface area, E_B is the energy of the bulk, E_S is the energy of the surface, n is the number of atoms and E_{corr} is an energy correction based on the self-interaction of the species. The energy of carbonation, $E_{ads}(CO_2)$, can then be calculated from (6)

$$E_{ads}(CO_2) = \frac{E_S(\text{modified}) - E_S(\text{pure})}{n_{CO_3^{2-}}} + E_{corr}\left(CO_3^{2-}\right), \qquad (6)$$

where E_S(modified) is the energy of a carbonated surface, and E_S(pure) is the energy of the pure surface before carbonate addition.

The calculation of free energies, A_s, can then be estimated by calculating the energies of many configurations and is expressed relative to the minimum energy for each coverage, $E_{S_{min}}$, given by (7)

$$A_S = E_{S_{min}} - RT \ln(Q), \qquad (7)$$

where Q is the total partition function summed over all surfaces for a given carbonate addition method and orientation, given by (8)

$$Q = \sum e^{\left(-E_S - E_{S_{min}}/RT\right)}. \qquad (8)$$

The free energies can then be substituted into (5) and (6) allowing the surface free energy and free adsorption energies to be calculated, respectively. In addition, the average surface energy can be estimated using the statistical mechanical expression shown by (9)

$$\langle\gamma\rangle = \frac{\sum \gamma_i e^{\left(-E_S - E_{S_{min}}/RT\right)}}{Q}. \qquad (9)$$

This requires only that we sample sufficient numbers of different configurations, which is possible using the

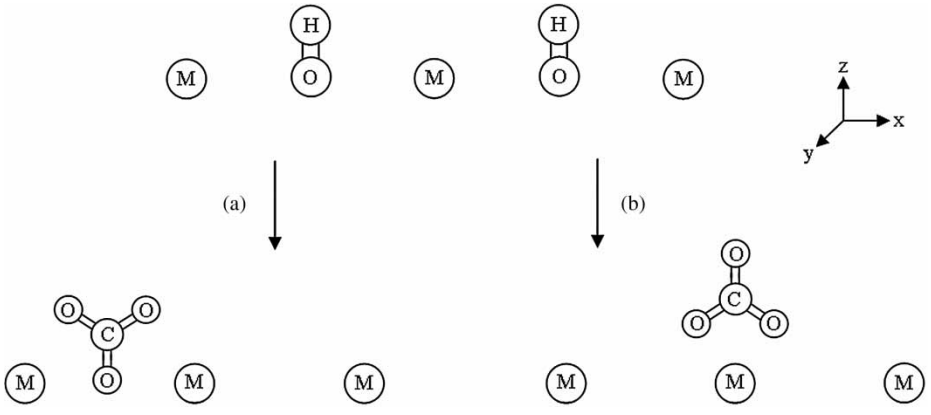

Figure 3. Simplified schematic showing the methods for carbonating the surfaces of $Ca(OH)_2$ and $Mg(OH)_2$. Method (a) shows replacement of a surface OH to place the carbonate *into* the surface, followed by removal of a further OH to balance charges. Whereas method (b) shows removal of two surface OH groups followed by carbonate placement in a bidentate manner *above* a surface metal atom. Atoms labelled M refer to either calcium or magnesium.

simple interatomic potentials. For hydration, the calculation of surface and adsorption energies is identical to the above method, except that $n_{CO_3^{2-}}$ becomes n_{H_2O} and $E_{corr}\left(CO_3^{2-}\right)$ is changed to $E_{corr}(H_2O)$.

The correction term used in (5) and (6) accounts for the self energies of the species and is different for each species added to the surface. The calculation of the correction factor was done in a similar way as used by de Leeuw et al. [38]. However, for surface carbonation, from gaseous CO_2, it represents the following reaction:

$$M^{2+}_{(g)} + 2OH^{-}_{(g)} + CO_{2(g)} \rightarrow M^{2+}_{(g)} + CO^{2-}_{3(g)} + H_2O_{(g)}, \quad (10)$$

where M^{2+} can be either magnesium or calcium. For the $Mg(OH)_2$ calculations, a correction factor of 29.27 eV was used, whereas for $Ca(OH)_2$ the value was 30.04 eV. When considering liquid water, $E_{corr}(H_2O)$ includes the self-energy of an isolated water molecule, -9.1 eV, and the heat of vaporisation, -0.45 eV.

The carbonated surfaces in this study were modelled using previously derived potentials. The hydroxide model is a form of the Baram and Parker [39] potential, derived for looking at hydrogen defects in α-quartz and sodalite surfaces and in the hydroxide crystal structures of $Mg(OH)_2$ and $Al(OH)_3$, and has also been successfully used to model goethite surfaces [40]. The calcium hydroxide interactions are from the work of Kerisit et al. [36], modelling the dissociative adsorption of water on calcium carbonate surfaces. The carbonate model was derived by Pavese et al. [41] to reproduce structural properties, elastic constants and vibrational frequencies of calcite (calcium carbonate), whereas the water model is that of de Leeuw and Parker [42] which was derived to have both a polarisable oxygen atom as well as being compatible with the Baram and Parker hydroxide potentials.

3.2.2 *Adsorption and surface alteration*

The adsorption of carbonate and water was modelled on five significant low energy magnesium and calcium hydroxides surfaces. The relaxed and unrelaxed surface energies (Table 4) show that, for the two materials, the relaxed surface energies have the same relative stability from the most to least stable of $\{001\} > \{102\} > \{101\} > \{201\} > \{100\}$. This trend is also mirrored by the unrelaxed surface energies.

The surface free energies and adsorption energies, Figures 4 and 5, respectively, for the adsorption of a single carbonate molecule on the two materials show that carbonation is generally an unfavourable process on these surfaces. This is particularly true for the magnesium hydroxide surfaces, where carbonation causes an increase in the surface energies. In addition, energies of adsorption for these processes are endothermic, therefore making the surfaces of brucite unsuitable for direct carbonation, which agrees with Churakov et al. [37]. The majority of equivalent calcium surfaces also show a degree of surface destabilisation, with associated endothermic adsorption energies, as a result of surface carbonation. Additionally, the carbonated surface energies of $Mg(OH)_2$ are all higher in energy than those of $Ca(OH)_2$, in accordance with the trend in pure surface energy. However, two of the calcium hydroxide surfaces show favourable adsorption of carbonate, namely $\{101\}$ and $\{201\}$ surfaces. This indicates that the direct carbonation of portlandite is spontaneous; making this material more suitable for use in carbon sequestration. Further analysis of these surfaces shows that the method of carbonation giving rise to the lowest energy surface structures differs for the two surfaces, with $\{101\}$ surface having lower surface energies via replacement of a hydroxide *into* the surface, whereas the favourable method for {201} was via addition *above* a surface Ca ion.

The hydrated surface free energies and adsorption energies are shown in Figures 6 and 7, respectively, with the results indicating that hydration is energetically favourable for all the surfaces. The exception to this is $\{001\}$ surface, which, despite it being an exothermic process, increases the surface energy, thereby indicating the surface's hydrophobic nature. In addition, the relative stabilities of the surfaces remain the same, with the $Ca(OH)_2$ surfaces being lower in energy than their magnesium equivalents.

The change in the average surface free energies, from the pure surface energy, produced by the adsorption of either a single carbonate or water for the modelled surfaces

Table 4. Unrelaxed and relaxed surface energies of the modelled surfaces of $Ca(OH)_2$ and $Mg(OH)_2$.

	$Ca(OH)_2$		$Mg(OH)_2$	
Surface	Unrelaxed surface energy (J/m^2)	Relaxed surface energy (J/m^2)	Unrelaxed surface energy (J/m^2)	Relaxed surface energy (J/m^2)
{001}	0.03	0.06	0.06	0.03
{100}	0.84	1.20	1.20	0.51
{101}	0.63	0.87	0.87	0.45
{102}	0.52	0.72	0.72	0.35
{201}	0.74	1.05	1.05	0.50

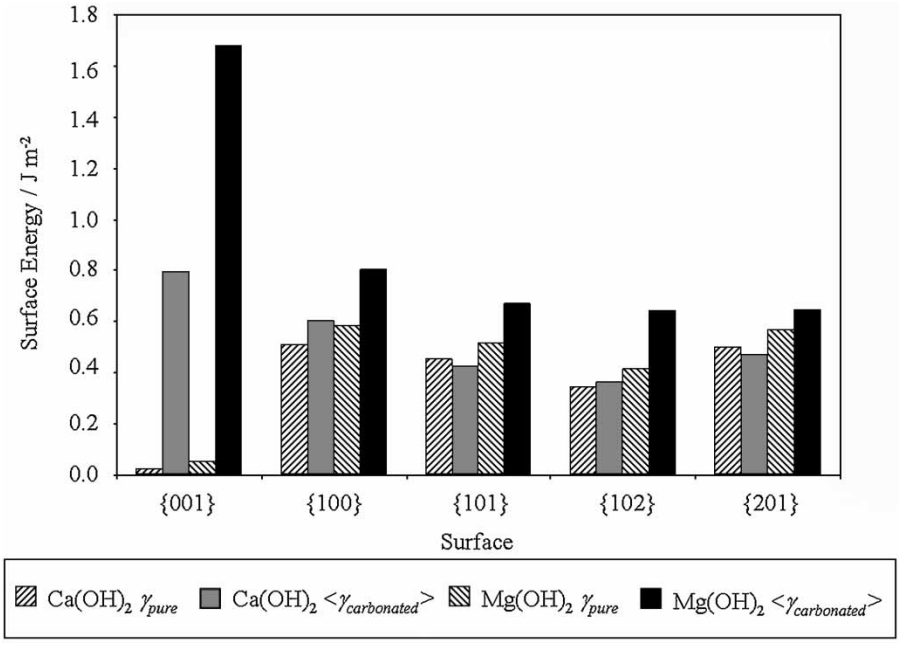

Figure 4. Bar plot to show the surface energies of the pure $Ca(OH)_2$ and $Mg(OH)_2$ surfaces, along with the average carbonated surface free energies for the adsorption of a single carbonate molecule.

are shown in Table 5. A positive value indicates surface stabilisation and negative value shows destabilisation. The data clearly shows that for both materials, hydration offers the greatest stabilisation of the surface, therefore being the most favourable process. However, this is not the case for the $Ca(OH)_2$ {1 0 1} and {2 0 1} surfaces. Here, the change in surface energy as a result of carbonation gives a small amount of additional stability to the surface.

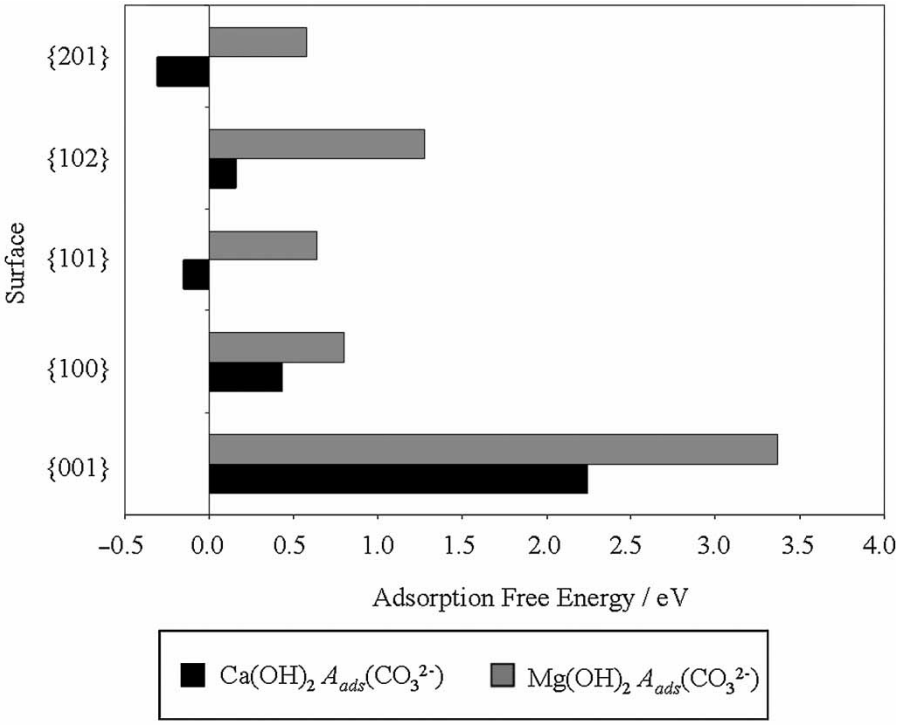

Figure 5. Average adsorption free energies of carbonation for the adsorption of a single carbonate molecule onto the surfaces of $Ca(OH)_2$ and $Mg(OH)_2$.

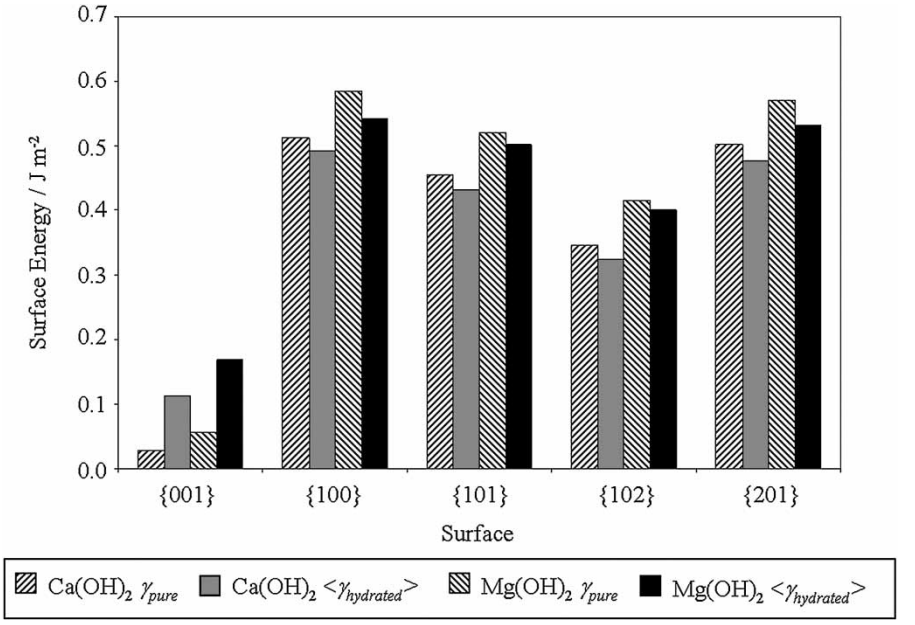

Figure 6. Bar plot to show the surface energies of the pure $Ca(OH)_2$ and $Mg(OH)_2$ surfaces, along with the average hydrated surface free energies for the adsorption of a single water molecule.

Although the stabilisation is not large, it indicates that the competition of water and carbonate on these surfaces should, at least, be favourable.

In summary, the adsorption of either a single carbonate or water molecule onto the low index surfaces of both magnesium and calcium hydroxide has been considered. Results indicate that the lowest energy surface of both materials, namely {0 0 1}, is unsuitable for the adsorption of either species, with both carbonation and hydration of the surface leading to surface destabilisation. The other surfaces of magnesium hydroxide modelled reveal similar results for carbonation, therefore suggesting the unsuitability of this material for direct carbon sequestration. The surfaces would therefore need to be modified, possibly

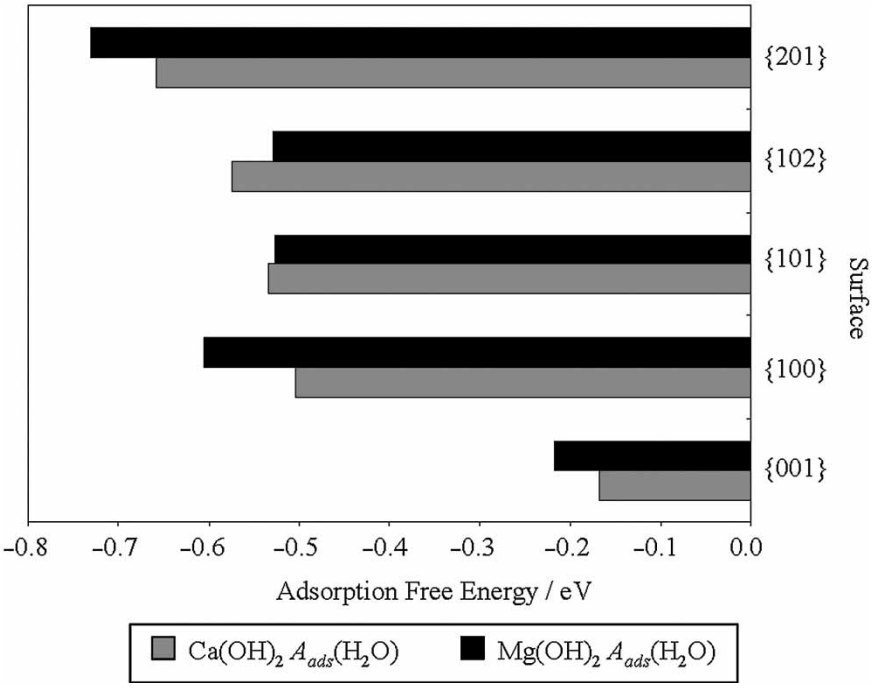

Figure 7. Average adsorption free energies of hydration for the adsorption of a single water molecule onto the surfaces of $Ca(OH)_2$ and $Mg(OH)_2$.

Table 5. Average change in surface free energy values from the pure surface energy upon the adsorption of a single carbonate, $\Delta\langle\gamma_{carb}\rangle$, and a single water molecule, $\Delta\langle\gamma_{hydrat}\rangle$, on the selected $Ca(OH)_2$ and $Mg(OH)_2$ surfaces.

	$Ca(OH)_2$		$Mg(OH)_2$	
Surface	$\Delta\langle\gamma_{carb}\rangle$ (J/m^2)	$\Delta\langle\gamma_{hydrat}\rangle$ (J/m^2)	$\Delta\langle\gamma_{carb}\rangle$ (J/m^2)	$\Delta\langle\gamma_{hydrat}\rangle$ (J/m^2)
{0 0 1}	−0.77	−0.09	−1.62	−0.11
{1 0 0}	−0.09	0.02	−0.22	0.04
{1 0 1}	0.03	0.02	−0.15	0.02
{1 0 2}	−0.02	0.02	−0.23	0.01
{2 0 1}	0.03	0.02	−0.08	0.04

by dehydroxylation, to make it more suitable. The results for the equivalent calcium surfaces are similar, although {1 0 1} and {2 0 1} surfaces show more positive results. These surfaces show not only that carbonation would be a favourable process, but also that they would compete for adsorption favourably with the physisorption of water molecules. Therefore, stabilisation of these surfaces, to increase their expression in resultant crystals, could lead to a possible material for carbon sequestration, although further simulation is required to confirm this. In addition, these results highlight the importance of modelling similar systems as trends cannot always be applied across all materials of the same class.

The next steps of this work will be to consider both the mixed adsorption of carbonate ions and water, as well as the adsorption of bicarbonate ions to assess how the adsorption is different to that of a simple carbonate. An additional study of interest would be to consider the co-adsorption of carbonate and charge-compensating ions. The realism of the simulation can be further increased using dynamical methods, which the next section concerns, focusing on the mineral–water interface by replacing the vacuum region by a slab of water. Initially the adsorption of carbonate to calcium oxide surfaces will be considered, before moving to silica surfaces to consider the adsorption of pollutants and the effects of extremes of pH on the resulting interface.

4. Molecular dynamics simulations of the mineral–water interface

4.1 Carbonate adsorption on calcium oxide surfaces

We used molecular dynamics simulations to probe related mineral–water interfaces, with and without surface carbonation. The high natural abundance of water means that it is essential to investigate the effect of water on processes and reactions which occur on mineral surfaces.

The system used in this study is that of calcium oxide. This has been used not least because there is a wealth of knowledge on this material but also as it acts as a model system for more complex higher oxides, such as silicates and hydroxysilicates. The aim of this work is to help understand the nature of the CaO–water interface and to demonstrate how the structure of the surface may influence the water structure and how it affects the diffusion and transport properties of adsorbing ions at the surface.

The potentials used to model the CaO surface in contact with both the water and carbonate are the same as used for the carbonation and hydration of the surfaces of portlandite. The model used for simulating the calcium oxide component of the simulations were those of Catlow and Lewis [43], where the oxygen is modelled with a polarisable shell and was empirically fitted to reproduce experimental structures, lattice constants, elastic and dielectric constants.

The methodology of generating the carbonated slabs is similar to that outlined for the addition of carbonate groups to hydroxide surfaces, where all combinations from one carbonate to monolayer coverage were considered to find the lowest energy surface structure. This surface was then used to generate a slab, which was carbonated on only one side. A layer of water, approximately 20 Å in depth was then added to the carbonated surface, leaving a vacuum gap of approximately 20 Å. This was then modelled using molecular dynamics for 1 ns, or until energy convergence was seen. The vacuum gap was introduced to prevent potential problems resulting from possible residual pressure in the system, which can occur as a consequence of using the NVT ensemble. The generation of a dipole by carbonating a single side of the slab was deemed to be negligible due to; firstly, the size of the cells used in the simulations, and secondly, as the high dielectric constant of the water layer would dampen the effect of the dipole.

The surfaces studied in this manner were {1 0 0}, {1 1 1} and {3 1 0} surfaces. The {1 0 0} was used as it is the most stable surface of calcium oxide; having a structure of a 'perfect', flat surface. The {3 1 0} is related to {1 0 0} by the surface structure consisting of {1 0 0} terraces, separated by steps, thereby allowing the influence of steps on the {1 0 0} to be considered. The {1 1 1} surface is a polar surface; therefore its inclusion allows us to consider different surface configurations. The carbonate concentrations for the lowest energy slabs were 4.33, 5.00 and 9.57 CO_3^{2-}/nm^2 for {1 0 0}, {1 1 1} and {3 1 0} surfaces, respectively, indicating that {3 1 0} surfaces take up the most carbonate per unit area out of the three modelled surfaces.

4.1.1 The structuring of water above pure and carbonated CaO surfaces

We started by examining the structure of water above the pure, un-carbonated surfaces by analysing both the average density in both the *z*-direction of the cell and by plotting the average water density in the simulation cell. The average water density relative to the density at the

position z_0 is defined by (11) [44]

$$\rho(z) = \frac{\langle n(z) \rangle}{n(z_0)}, \tag{11}$$

where $n(z)$ and $n(z_0)$ are the number of water molecules at a position z and z_0, respectively. In these calculations, z_0 was taken to be the maximum distance from the surface. The plots of both the water density profile and z-density are shown in Figure 8(a)–(c) for the pure {1 0 0}, {1 1 1} and {3 1 0} surfaces of CaO, respectively.

The average water density results show that water layering is evident on all surfaces. However, the structure of the layering is different for each surface. The {1 0 0} surface forms flat sheets of coordinating water, with an initial calcium–water oxygen distance of ~2.4 Å. The layers then continue away from the surface in the z-direction, at regular spacings of ~2.5 Å between the oxygen atoms of water until the density becomes more bulk-like with no clear structure.

The water structure above {1 1 1} surface consists of rows of coordinated water sited at the equivalent lattice positions of the oxygen, extending into the water layer for about four layers. The layer immediately above the surface contains water in distinct crystallographic sites with an ice-like structure. This is different to the continuous flat sheets observed for {1 0 0} surface. The z-density profile also shows that there is more mobility on the surface, with some of the surface calcium atoms mixing with the water close to the surface. The water structure above {3 1 0} is similar to that above {1 1 1} surface, where the coordinated water is in rows above the surface rather than in flat sheets. For this stepped surface, coordinated molecules in distinct crystallographic sites are present around the step, whereas the density seen above {1 0 0}-like terrace is more smeared, in a similar manner to the sheets of water seen above {1 0 0} surface. Additionally,

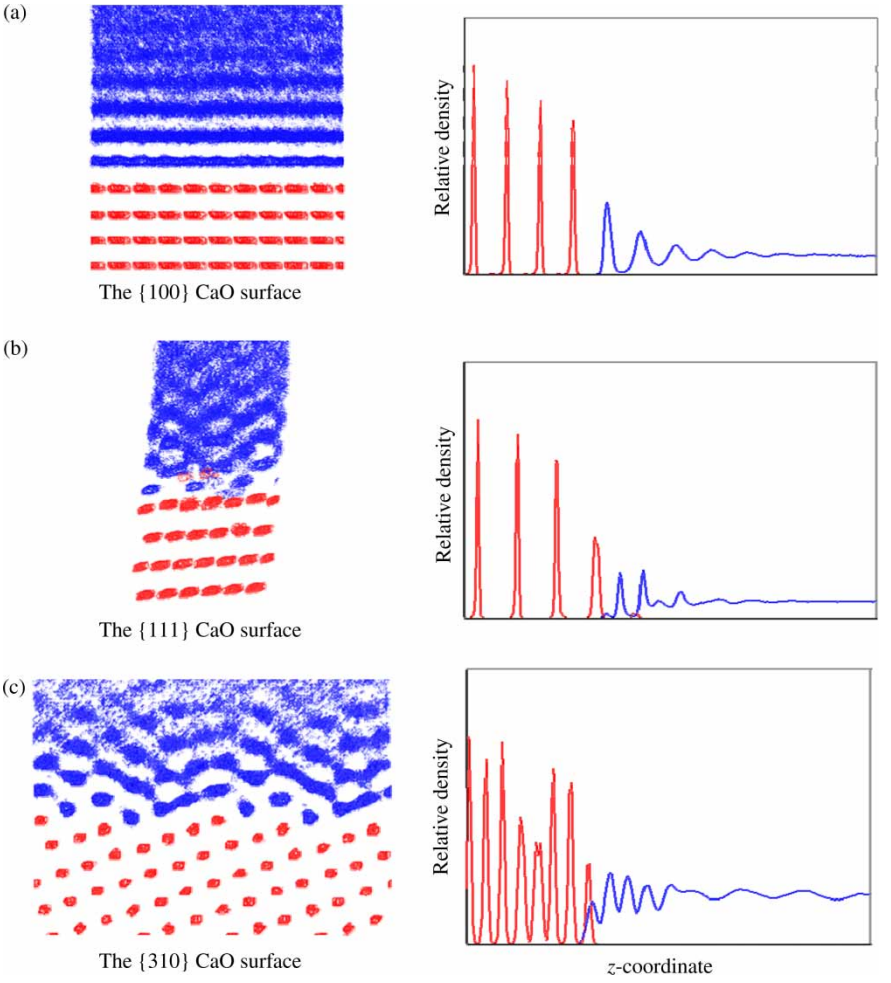

Figure 8. Density plots showing average densities of calcium (coloured red) and the oxygen of water (coloured blue) at the mineral–water interface and z-density plots for (a) the {1 0 0}, (b) the {1 1 1} and (c) the {3 1 0} CaO surfaces. Note: For the plots of water density, only regions of high water density are shown and the slight smearing of calcium density is caused by their vibration on their lattice positions.

the z-density profile shows the formation of four to five coordinated water layers above the surface. It should be noted that the Ca density peaks form a different structure purely because of the orientation of the CaO layers are not perpendicular to the z-axis.

To assess the mobility of water in the first coordinated water layer above the surface, we can determine residence time for the water. This is defined as the average amount of time a water molecule spends in the first hydration shell of a calcium atom, defined as being 3.25 Å, and can be calculated from the residence-time correlation function, Equation (12), as given by Impey et al. [45]

$$\langle R(t)\rangle = \left\langle \frac{1}{N_0}\sum_{i=1}^{N_t}\theta_i(0)\theta_t(t)\right\rangle, \tag{12}$$

where N is the number of water molecules in the first hydration shell, $\theta_i(t)$ is the Heaviside function, which is 1 if the ith water molecule is in the first hydration shell at time t and 0 otherwise. A water molecule is only counted as having left the first hydration shell if it has done so for at least 2 ps, thus allowing a water to leave the first hydration shell and return, without entering the bulk, for a significant amount of time and still be counted. The residence time can then be obtained by the integration of $\langle R(t)\rangle$ using (13)

$$\tau = \int_0^\infty \langle R(t)\rangle \mathrm{d}t. \tag{13}$$

The residence time can help identify both the mobility of water on the surface, as well as the relative strength of the coordination. The residence time for water on {1 0 0} surface is 8 ps, indicating that the coordination of water is weak and that it remains mobile through the simulation. However, the residence time of a water–oxygen coordinating to a calcium on {1 1 1} surface is significantly higher at 797 ps, nearly as long as the 1ns simulation length, thus indicating a strong coordination of water to the surface, holding the water fixed in the layered rows directly above the surface. The {3 1 0}, follows the water density profile in that it varies across the surface. This is shown by Figure 9, which shows the residence time between a surface calcium ion and a water oxygen as a function of the x-coordinate.

The lowest energy surface of {3 1 0} consists of terraces with uneven lengths between the steps. The steps have a height of approximately 2.3 Å and the terraces have lengths of approximately 4.6 Å and 9.1 Å. The density profiles, Figure 8(c), show stronger water coordination around the step edge than on the terraces, which is also reflected by the residence times. However, the residence times above the two different length terraces are different. The shorter 4.6 Å terrace continues to have strongly coordinated water above it, more likely a consequence to the proximity of steps at either ends of it. The longer 9.1 Å terrace, however, shows that the waters present adjacent to the steps are bound more strongly than those in the centre of the terrace. In addition, the water coordination in the centre of the longer terraces more closely resembles those of {1 0 0} surface in magnitude.

Similar density profiles can be calculated for the carbonated surfaces, shown in Figure 10, where the surfaces effectively consist of a one unit deep layer of calcium carbonate on the CaO surface. All three surfaces

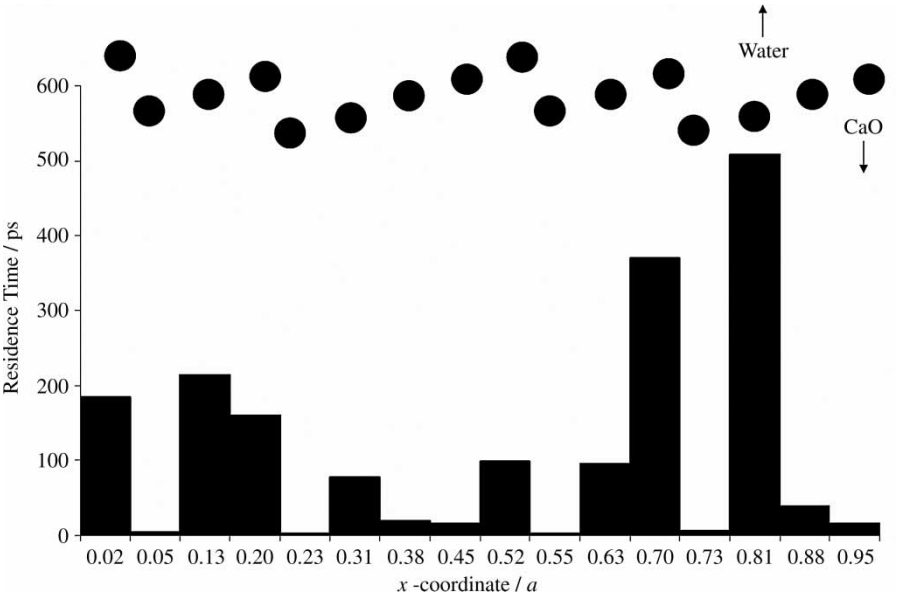

Figure 9. Plot showing the residence times between a surface calcium ion with the oxygen of a water molecule as a function of the x-coordinate / the a lattice parameter (30.402 Å) of the calcium ion on the {3 1 0} CaO surface. The structure of the step is also overlaid for reference.

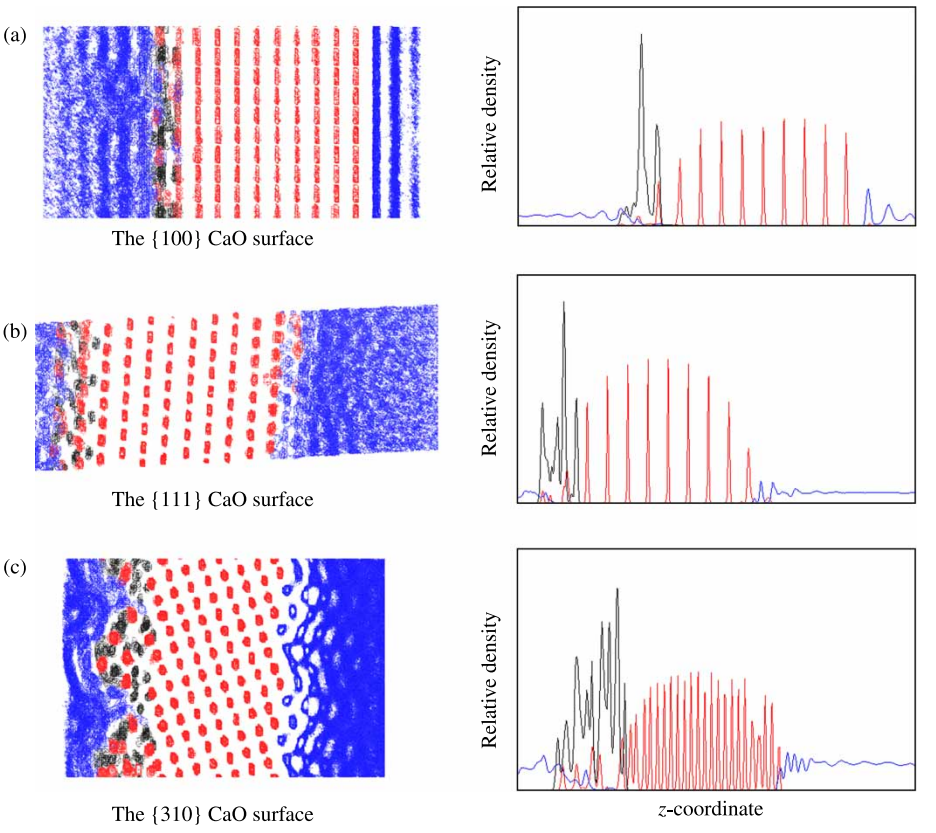

Figure 10. Density plots showing average densities of calcium (coloured red) and the oxygen of water (coloured blue) and carbonate (coloured black) at the mineral–water interface and z-density plots for (a) the {1 0 0}, (b) the {1 1 1} and (c) the {3 1 0} CaO surfaces. Note: the smearing of calcium density is due to vibration of the calcium atoms upon their lattice sites during the simulation.

differ from the equivalent pure surfaces. In particular, the distinct water layering seen for the pure surfaces is either lost or severely disrupted by the presence of the carbonate layer. The {1 1 1} surface shows complete removal of the layering, with the density resembling a more bulk-like value whereas {1 0 0} shows some weak layering remaining above the surface, with areas of concentrated water present, forming a coordinated unit rather than a distinct layer. The {3 1 0} surface, however, undergoes a reconstruction upon carbonation, prior to the molecular dynamics simulation, which is evident from the density plots in Figure 10(c). Whereas the pure surface comprised of single unit steps, separated by alternate long and short terraces; the carbonated {3 1 0} surface shows a rearrangement to give a more ordered step arrangement. This comprises of steps which are two units deep and terraces which are the same length between the steps across the surface. This regularity is then passed to the water layer, although to a lesser degree than evaluated for the stochiometric surface. The weak layering seen immediately above the surface is smeared, indicative of a mobile water layer, causing the average density to form a layer, in a similar manner to the highly mobile layers above the pure {1 0 0} surface.

Differences between the carbonated and pure surfaces are also evident from the water residence times. In addition to the average amount of time a water molecule spends within the first hydration shell of a surface calcium ion, we can also consider the water residence time on a carbonate group, which is via a hydrogen bonding interaction to a carbonate oxygen. The residence time for a water coordinating to a calcium in the second layer from the surface will also give insight into both the penetration of water into the carbonate, as well as its mobility whilst there. Table 6 details the residence times for {1 0 0} and {1 1 1} surfaces.

The residence times for {1 0 0} surface show that the water mobility is reduced from that of the pure surface, this is most likely due to the roughening of the surface, making it easier for water to coordinate around exposed calcium

Table 6. Residence times, τ, for water above carbonated surfaces for the {1 0 0} and {1 1 1} surfaces at different sites above the surface.

Surface	τ Ca···OH_2 (on surface, ps)	τ Ca···OH_2 (below surface, ps)	$\tau^{2-}[O_2CO]$ ···HOH (ps)
{1 0 0}	228	152	85
{1 1 1}	602	5	101

ions than when on the flat surface. It is also seen that water does indeed penetrate into the carbonate layer and the coordination is noticeable. However, the water coordination at the surface, forming the density profile seen in Figure 10(a) is due mainly to the calcium as opposed to the carbonate itself. This is reflected by the shorter residence time around the carbonate, indicating an increased mobility of water and hence weaker coordination. In comparison, the carbonated {1 1 1} surface shows a considerably longer residence time, indicating better coordination. However, as with {1 0 0} surface, the residence time of the pure {1 1 1} surface is larger than the carbonated form which is indicative of the carbonation causing similar surface disruption, resulting in an increase in water mobility.

Figure 11 shows a simplified schematic of {3 1 0}surface layer, along with the residence times across the surface as a function of the *x*-coordinate of the ion in question, with both τ Ca$\cdots$OH$_2$ and τ^{2-}[O$_2$CO]$\cdots$HOH being considered. The results suggest there is strongly bound water in the position inside the step which remains coordinated for the majority of the simulation, in this case 2ns. The residence times are calculated for individual ions, rather than an average for the row, so although there is no evidence of the same coordination inside the other step, this may not be true further along the row in the *y*-direction However, with the exception of this site, it can be seen that the coordination along the terraces has comparable residence times with those seen at the carbonated {1 0 0} surface. Additionally, for this surface, little or no water penetration into the carbonate layer was seen.

Overall, the results indicate the presence of water layering occurring on the modelled low index CaO surfaces. On the pure surfaces, this layering is seen to four to five layers into the bulk. Flatter surfaces give rise to diffuse layers with no clear coordinated sites. However, surface features, such as steps, can directly influence the water layer causing the formation of localised regions of water coordination, sometimes with water occupying distinct crystallographic sites, and an associated decrease in water mobility at those points. The importance of this is that when considering surface adsorption processes, the nature of the water structure directly above the surface can impact on the energetics and diffusivity of the incoming adsorbate, to either coordinate to or react with the surface. The addition of carbonate onto the surface, effectively creating a surface layer of calcium carbonate, also has a dramatic effect on the water structure, mainly by disrupting and reducing this layering, which would have a significant impact on the surface properties.

An important extension to this work is to study the adsorption mechanisms, for example, through the use of potential of mean force calculations which will yield the free energy profiles. The next section will detail some work which begins to consider this for the adsorption of pollutants on the quartz surface. We will then discuss the diffusion properties of siliceous zeolite–water interfaces,

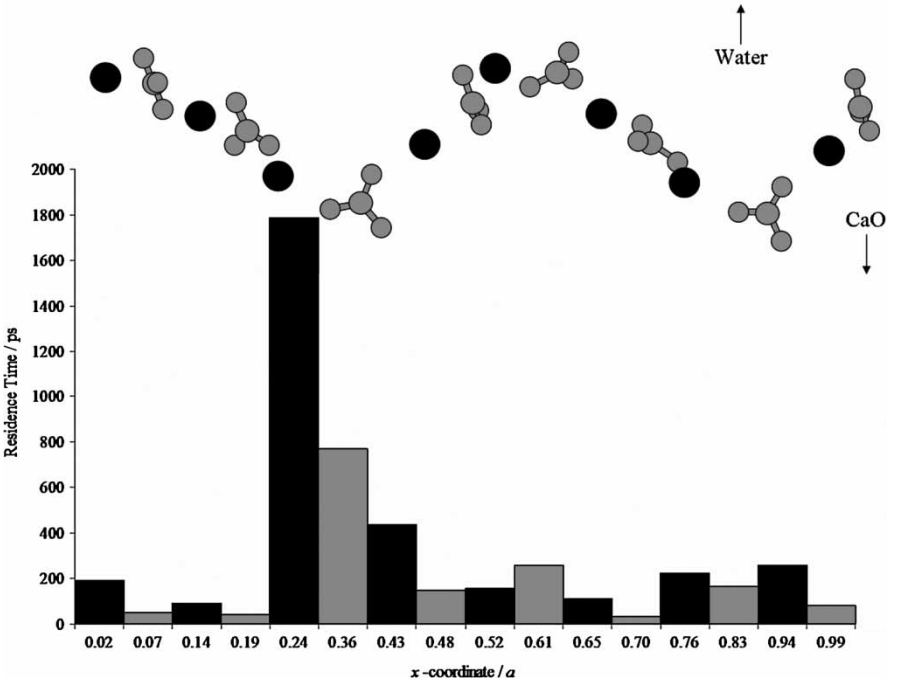

Figure 11. Plot of the residence time between a water oxygen and a calcium atom (black) and between the oxygen of a carbonate with the hydrogen of water (grey) as a function of the *x*-coordinate/the *a* lattice parameter (30.402 Å) for the atom in question. The structure of the uppermost layer at the surface is also included for reference.

which could equally be done to further our knowledge above pure and carbonated CaO surfaces.

4.2 The adsorption of TCDD at the quartz–water interface

The modelling of the adsorption and transport properties of pollutants in the environment is an important and highly active area of research. One such range of pollutants, found in soils, are PCDDs (polychloro-dibenzo-*p*-dioxins). PCDDs are important to study due to their high toxicity. They have been detected in the food industry and are linked to industrialisation and waste incineration. However, both their origin and the role minerals play in trapping, synthesising and destroying PCDDs are still unclear. Furthermore, there is no experimental data available to determine the diffusivity or adsorption and desorption energies as a function of chlorine content, mineral surface, pH or temperature. Therefore, simulations have the potential to give important insights into understanding and prediction of the relative importance of these different factors.

We report recent work on the adsorption of TCDD (2,3,7,8-tetrachloro-dibenzo-*p*-dioxin), which is the most toxic [46] of the 75 PCDD congeners on the surfaces of α-quartz, in order to understand the role played by the surface structure and the solvent. Quartz was chosen as a substrate because it is the most abundant mineral in the Earth's crust and its role in the adsorption and formation of PCDDs on soils is unknown. The simulations utilise both static lattice minimisations and molecular dynamics simulations to characterise the adsorption energies of TCDD as well as its mobility on the surface, both in the presence and absence of water. These dynamical properties offer data at the atomic scale to assist in the understanding of macroscopic observations, such as adsorption and desorption processes as well as diffusivity. An additional benefit of these simulations is that they provide information on the surface properties and their interactions with solvent molecules, in this case water.

The potential model of Sanders et al. [47] was used to model the silica surfaces, with the Baram and Parker [39] potential for the surface hydroxide ions. The water model is that of de Leeuw and Parker [42], with an adjusted hydrogen-bond potential of Kerisit and Parker [48]. These potentials have also been used in previous studies, for example, the models have been shown to reproduce the structural and dynamical properties of quartz and its surfaces [38,49,50]. When modelling molecules, such as PCDD, on quartz surfaces, we need a model for the internal motions. We found the simple Dreiding model [51] force field adequate for this essentially rigid molecule and used the CVFF [52] for the intermolecular interactions. The calculation of hydroxylated surface energies was done in a similar method outlined for the calculation of carbonated surface energies. The value of the correction factor for the hydroxylation process was calculated to be -7.72 eV per water molecule.

4.2.1 Results of water structuring and TCDD adsorption

The unit cell of α-quartz is hexagonal and is modelled with the $P3_121$ space group and lattice constants of $a = b = 4.91$ Å and $c = 5.41$ Å [53]. The most commonly exposed surfaces of α-quartz are {10.0}, {11.0} and {11.2}, thereby we have elected to study the adsorption process using {10.0} and {11.0} surfaces, with surface hydroxylation present to stabilise the under-coordinated surface silicon atoms.

The lowest energy {10.0} surface has a surface energy of 0.44 J/m^2 and contains only vicinal OH groups, with a surface concentration of 7.65 OH/nm^2. The hydroxylated {11.0} surface, with a surface energy of 0.49 J/m^2, requires a higher surface concentration of 8.82 OH/nm^2, comprising of a mixture of geminal and vicinal groups. Following the work of Fubini et al. [54], in which surface hydrophilicity is related to type of hydroxyl groups, we would expect {10.0} surface of α-quartz to be more hydrophilic than {11.0} surface because it only has vicinal OH groups. Examination of the water structure, Figure 12(a) reveals a higher degree of water ordering on {10.0} surface of silica, with the surface adsorbed water molecules orientated perpendicular to the interface.

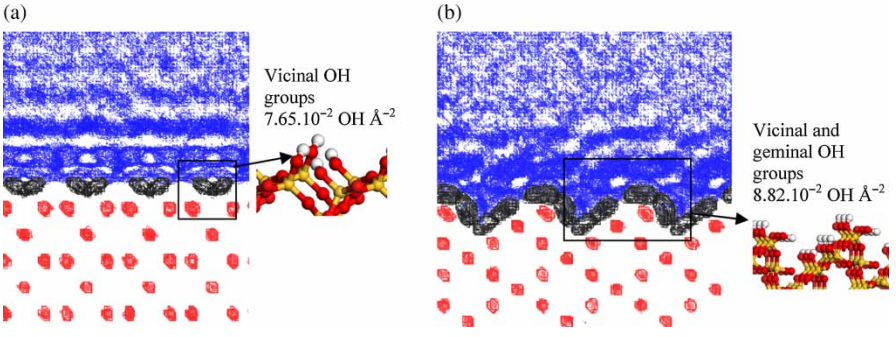

Figure 12. Water ordering on the (a) {10.0} surface and (b) {11.0} surface of α-quartz. The water is represented by blue, the hydrogen of surface hydroxyl groups by black and the α-quartz by red.

Conversely, the water molecules lay flat at {11.0} interface creating more distortion of the water layering, Figure 12(b). A further difference seen is the diffusion of water on the surface, measured using mean square displacement data. The diffusion on {10.0} surface, $2.7 \times 10^{-9}\,m^2/s$, is measured as slower than on {11.0} surface, $2.9 \times 10^{-9}\,m^2/s$, reflecting the relative hydrophilicity of the two surfaces.

We can then compare the adsorption of TCDD on the two hydroxylated surfaces. It can be seen from the results, Table 7, that the adsorption of TCDD on {10.0} surface is slightly stronger, by 0.16 eV, than {11.0} surface. The orientation of TCDD on the surfaces was also seen to be flat.

PCDDs are insoluble in water, with the solubility of TCDD being 16.3ppt [55]. The interaction of TCDD with a slab containing 710 water molecules shows that the diffusion of TCDD in pure water is unfavourable. The dioxin remains on the surface, at the water–vacuum interface, with an adsorption energy of -0.72 eV and a similar diffusion coefficient to water (TCDD at $3.5 \times 10^{-9}\,m^2/s$, water at $3.6 \times 10^{-9}\,m^2/s$). When the dioxin is placed at a mineral–water interface though, its interaction differs depending on the surface. At the hydrophilic {10.0} surface, the TCDD is not seen to adsorb, whereas the TCDD remains flat on {11.0} surface, with a diffusion coefficient of $0.49 \times 10^{-9}\,m^2/s$. This phenomenon is caused by be the competition of water and dioxin and the nature of the surface of the mineral.

In summary, we have compared two different surfaces of α-quartz and the resultant adsorption of TCDD. The results indicate that the adsorption/desorption is linked to both the surface state and the presence of solvent. With the work showing quantitatively the effect of the surface hydrophilicity as indicated by the hydroxylation to surface mobility of the pollutant.

4.3 The structuring of water above zeolite surfaces and the effects of pH

In addition to quartz, silica also has the ability to form porous materials, in the form of zeolites, through the use of templating materials. Prior to modelling the adsorption of complex adsorbates on the surfaces, such as TCDD, we first need to gain an understanding of the structure of these porous surfaces, as well as the interaction with water.

Table 7. Adsorption of TCDD on dry α-quartz surfaces, energies are for infinite dilution from the free gaseous molecule.

	{10.0} Surface	{11.0} Surface
Hydroxyl concentration (OH/nm^2)	7.65	8.82
E_{ads} (eV)	−1.37	−1.21
Distance (Å)	1.72	1.59

Further to this, the effects that pH and pH-determining ions have on the diffusion properties of the pores and surfaces is essential, as this will be affected by the region directly above it.

We elected to study siliceous zeolite A (LTA). The structure of LTA is cubic, with the *Fm-3c* space group and a lattice parameter of 23.69 Å [56]. The zeolite framework in LTA, shown in Figure 13, consists of two secondary building units: truncated octahedra, referred to as either β or sodalite cages, and double four-rings (D4R). This framework forms a three dimensional system of channels. The linking of the β-cages and D4Rs create large voids in the structure, called the α-cages, which are connected by 8-member rings (8R).

4.3.1 Methodology

The potentials used for the study of the zeolite surfaces are the same as used for quartz, which have been previously applied successfully for zeolites [57–59] and the zeolite A–water interaction [60]. The hydronium ion in this work was modelled using a modified water potential, where the oxygen shell charge was adjusted to give a total charge +1. The reduced polarisability of the hydronium oxygen is reflected by the reduction of the Buckingham *C* parameter, and Lennard-Jones *B* parameter, which both describe the interatomic induced polarisability. The potential parameters for this ion and its interaction with water, hydroxide and chloride ions are given in Table 8.

Molecular dynamics simulations were employed to study the mineral–water interface for LTA. For these calculations, a 22.8 Å {1 0 0} slab of siliceous LTA was generated with a surface termination consisting of D4Rs. The choice of surface termination was motivated by the observations of Sugiyama et al. [61] and Wakihara et al. [62], which found suggestive evidence, using AFM and HRTEM techniques, of D4Rs being exposed on {1 0 0} surface. An unsymmetrical slab was used, enabling the study of two surfaces simultaneously. One side of the slab had the D4Rs parallel to the surface (D4R-f, face) whilst the other had them perpendicular to the [100] direction (D4R-e, edge). The slab was initially optimised by static lattice

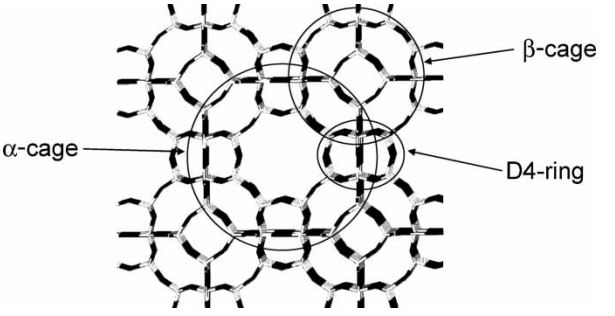

Figure 13. The structure of the siliceous zeolite LTA, grey represents the silicon atoms and black those of oxygen.

Table 8. Potential parameters used to model a H_3O^+ ion.

Core-shell parameters				
Ion	Core charge (e)	Shell charge (e)	k_2 (eV Å^{-2})	
O_T	1.25	−1.45	209.449602	
Buckingham potential parameters				
Ion Pair	A (eV)	ρ (Å)	C (eVÅ^6)	
O_T (S)–O (S)	22764	0.149	7.73	
O_T (S)–O_H(S)	22764	0.149	7.73	
Morse potential parameters				
Ion pair	A (eV)	B (Å^{-1})	r_0 (Å)	Coulombic subtraction (%)
O_T (S)–H_T	6.203713	2.220030	0.92367	50
Lennard-Jones (12,6) potential parameters				
Ion pair	A (eV Å^{12})	B (eV Å^6)		
O_T (S)–O_W(S)	39344.98	21.075		
O_T (S)–O_T (S)	39344.98	10.54		
n-m potential parameters				
Ion pair	E_0 (eV)	n	m	r_0 (Å)
O_T (S)–H_T	0.0112219	12	6	3.90698
Three-body potential parameters				
Ion group	k_{ijk} (eV/rad^{-2})	Θ_0 (°)		
H_T–O_T–H_T	4.199780	108.693195		

The different oxygen atoms are labelled as H_3O^+ (O_T), a lattice oxygen (O), an oxygen of a water (O_W) and hydroxide (O_H). The H_3O^+ hydrogen (H_T) is modelled in an identical way to that of a water molecule.

minimisation using METADISE, giving the same surface energy for the two surfaces of 0.15J/m^2. Water was then introduced by the placement of a 10 Å film of water on both sides of the LTA slab, as well as filling the cages and channels within the slab. A 20 Å vacuum gap was again introduced to one side of the simulation cell to prevent residual pressure with the NVT ensemble. The simulation was then run for a total simulation time of 3 ns.

Cleavage of silica surfaces leads to the exposure of under-coordinated silicon, making the surfaces of LTA highly unstable. To produce stable surfaces we therefore used the same methods employed for the α-quartz, through the hydroxylation of surface, via the dissociative adsorption of water. The concentration of surface silanols for the most stable surface is 2.85 OH/nm^2, which is true for both sides of the LTA slab.

4.3.2 *Results of the water structure, diffusivity and the effects of pH*

We can gain insight into the water structure around the LTA slab by calculating average density of water molecules throughout the simulation using that described for CaO surfaces. The water density profile for the LTA slab is shown in Figure 14. The density profile shows that the α-cages are empty, clearly highlighting the hydrophobic nature of the siliceous α-cages. Furthermore, water layering is seen throughout the simulation cell, with the layering reflecting the asymmetry of the slab. On the D4R-f side of the slab, the water layer close to the surface is seen to follow the curvature of the D4R, towards the channel aperture. Moreover, there is also clear water coordination within this layer, by high density sites where there is direct contact with the mineral surface, reflecting the crystal structure. On the D4R-e side however, the layers of water are seen to enter the open α-cages, becoming perpendicular to the surface. Evidence of water localisation inside the β-cages is also apparent.

It is also useful to consider the z-density of water in the simulation cell, as this can give a clear indication of any water layering which is seen in the cell. The z-density profile of water within {1 0 0} LTA simulation cell is given in Figure 15. The water density is seen to oscillate at both sides of the slab, as well as dropping down to zero inside the slab. There is again no clear evidence of water inside the α-cage, however, peaks are present on both sides of the 8R on the D4R-e side of the cell, indicating the presence of water inside the β-cage. The density on the D4R-f side decreases more rapidly than at the D4R-e surface, which is likely due to the presence of the open α-cages on the D4R-e surface of the slab. Layering is also stronger on the D4R-e surface. The maximum relative density on the D4R-e side of the slab reaches 1.67, whilst the maximum for the D4R-f side is

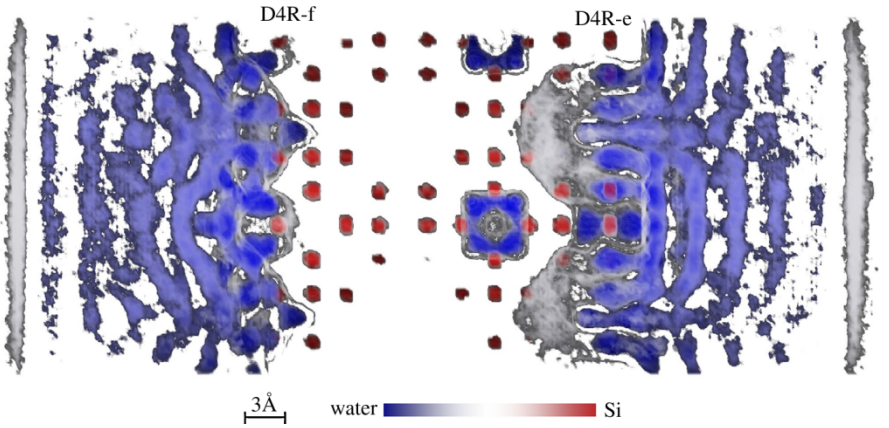

Figure 14. Water density profile around a {1 0 0} slab of siliceous LTA. Blue indicates are areas of high water density, light blue/grey indicates lower water density and red represent the density of silicon atoms.

equal to 1.32. Similarly, corresponding minima of density are also deeper on the D4R-e surface, reaching 0.56 for the D4R-e side compared to 0.76 for the D4R-f.

Another important quantity that can give further information on the water structure is the orientation order parameter, defined by Equation (14) [44]

$$S(z) = \left\langle \frac{1}{N_z} \sum_{i=1}^{N_z} \frac{1}{2} \left(3\cos^2\theta_i - 1\right) \right\rangle, \qquad (14)$$

where N_z is the number of water molecules at a distance z from the surface and θ is the angle between the molecular dipole moment and the normal to the surface. A value of S equal to -0.5 indicates that the water molecule is parallel to the surface, whereas an S value of 1 corresponds to the water molecular being perpendicular to the surface. As seen in Figure 16, we can plot the order parameter against the z-coordinate, along with the z-density profile for reference.

Water molecules at a distance away from the slab do not show significant ordering, although small oscillations correlating with the water density are present. However, in the regions both close to the surface and inside the open α-cage, S is seen to be negative. This indicates that the water orientation is closer to being parallel to the surface in these locations. However, this ordering is by no means as clear as has been reported for other materials, for example, calcite [63]. The presence of channels and cages significantly changes the geometry of the surface, thus the orientation parameter reflects the roughness of the surfaces.

The importance of the water ordering is that it can significantly modify the diffusion at the surface, therefore highlighting the importance of understanding the structure of water above surfaces to gain a true insight into diffusion

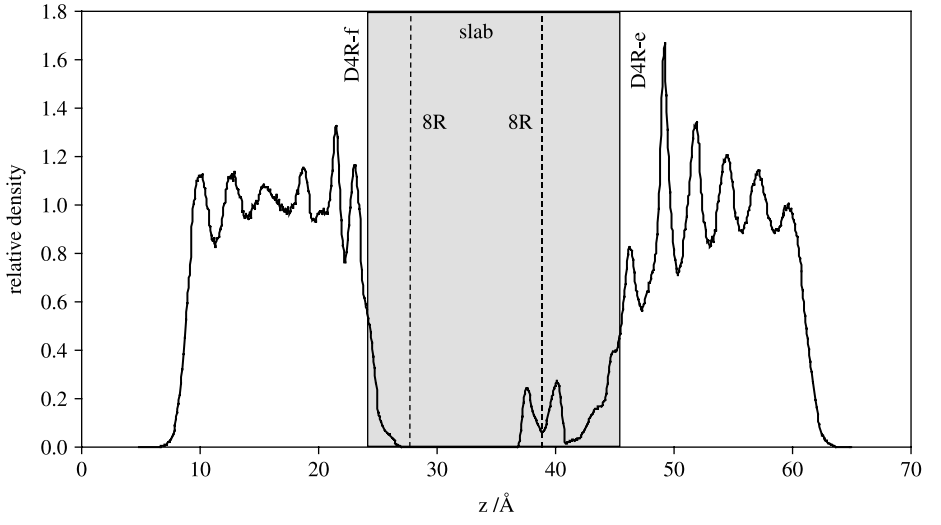

Figure 15. The z-density profile of water around a {1 0 0} slab of siliceous LTA. The position of the slab is indicated by the grey shaded region and the dashed lines show the positions of the 8-rings (8R) which delimit the α-cage.

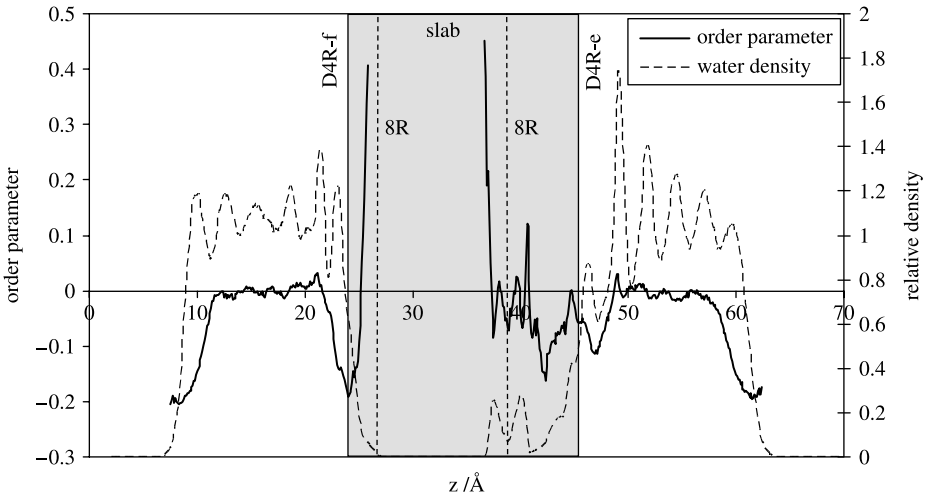

Figure 16. Plot of the orientation order parameter of water around a {1 0 0} slab of siliceous LTA, with the average water density against the z-coordinate.

properties. To assess this effect we can calculate the self diffusion coefficient in the directions both perpendicular, Equation (15), and parallel, Equation (16), to the surface. This is done using the mean square displacement [64]

$$D_z(z) = \frac{\lim_{t\to\infty} \langle (z(t) - z(0))^2 \rangle}{2t}, \tag{15}$$

$$D_{xy}(z) = \frac{\lim_{t\to\infty} \langle (z(t) - z(0))^2 \rangle}{4t}, \tag{16}$$

where z is a coordinate and t is the time. The results of the diffusion coefficients are shown in Figure 17, again with the water density profile for reference. It can be clearly seen than in both directions, the diffusion coefficients decrease as the distance to the surface decreases.

In the region close to the surface, both D_z and D_{xy} reach similar values, of approximately 1.0 and 1.2 $\times$ 10^{-9} m^2/s for the D4R-f and D4R-e surfaces, respectively. Outside the slab, D_z oscillates, correlating with the changes in water density at both the minima and maxima of the density. The oscillations are present throughout the water region, indicating that the distance from the surface is not large enough to reach bulk water properties. In contrast, the diffusion coefficient parallel to the surface, D_{xy}, does not show a match to the water density. This is a direct result of the water layering. Outside the slab, the water is ordered into distinct layers parallel to the surface, therefore implying that parallel diffusion will not be limited by the layering. However, inside the slab both diffusion coefficients show similar behaviour and are larger than their values outside of the slab. It can also be seen that D_z is larger than D_{xy} at the site

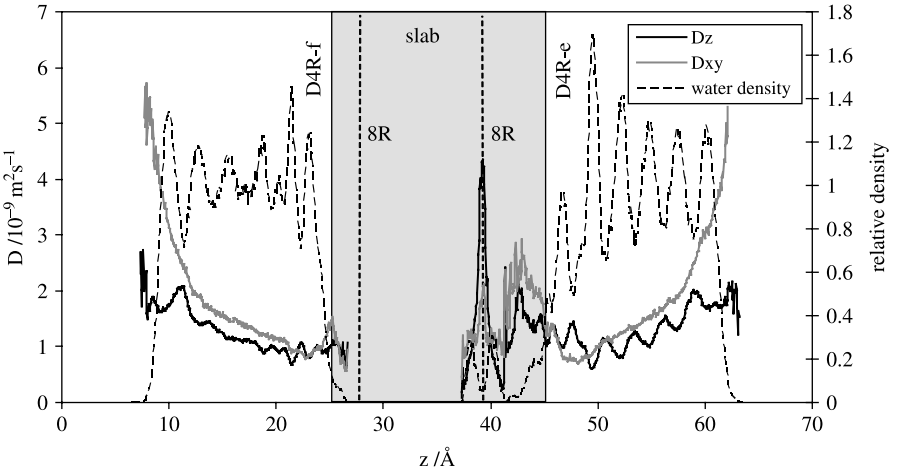

Figure 17. Plot showing the diffusion coefficients D_z and D_{xy} of water for a {1 0 0} slab of siliceous LTA against the z-coordinate of the system. The change in the water density with the z-direction is also shown for reference.

of the 8R as the 8R limits the movement of water in the parallel direction but not perpendicular to the surface.

When considering the nature of LTA surfaces in water it is also important to gain an appreciation of the effect that the pH of the solvent has on the surface properties. For this study we have considered the two extremes of pH. The pH of the system was set up through the addition of an appropriate number of H_3O^+ or OH^- ions, suitably compensated by Cl^- and Na^+ ions, respectively. The high extreme of pH was modelled by adding OH^- in a proportion of 1 OH^- per 55 water molecules, with an identical number of Na^+ to maintain charge neutrality, corresponding to a pH value of 14. An identical method was used for the addition of H_3O^+ ions, with the corresponding Cl^-, ions to generate a low extreme of pH of 0. We can then measure the diffusion coefficient of water in the direction perpendicular to the surface, D_z. The results of the diffusion coefficient data in the two extremes of pH is shown in Figure 18 alongside the simulation in neutral conditions for reference.

The plot also shows that the asymmetry of the slab has a strong influence on the diffusivity. The value of D_z has clear pH dependence in the D4R-f side of the slab where the solvent does not enter the slab by a large amount. The dependence seen is that the diffusion constant increases with increasing pH. The D4R-e side does not show this trend though, with the values of D_z for all pH conditions, being similar. In the open α-cage itself, D_z is larger for the high pH than for the other pH concentrations, reaching values of approximately $4 \times 10^{-9}\,m^2/s$. In the low pH solution, water is present in the α-cage only up to approximately 2.5 Å from the surface, therefore we are unable to calculate the value of D_z for some of the regions of the open cage at low pH conditions. Although not shown here, similar trends are seen for the D_{xy} data.

In addition, analysis of the distribution of the pH-determining ions in the low pH simulation, as seen in Figure 19, reveals that the H_3O^+ separates to the surface, followed by a layer of Cl^- ions. The adsorbed hydronium layer at low pH makes the surface positively charged, which would be expected for a pH below the point of zero charge, or the pH condition when the electrical charge density on a surface is zero. However, such separation is not present in high pH conditions, where the pH-determining ions form oscillating layers through the water layer rather than surface concentrated layers.

The layers of H_3O^+ and Cl^- ions at the surfaces seen in Figure 19 also have an effect on the orientation of water molecules. Figure 20 details the water orientation order parameter for the three different pH solutions as a function of the z-coordinate. It can be seen that for neutral and high pH solutions the results are very similar. However, for the low pH solution, the water orientation is seen to be perpendicular to the surface at approximately 3.0 Å away from the surface, which corresponds to the region between the layers of H_3O^+ and Cl^- ions.

In conclusion, this study of water structure has shown how the use of molecular dynamics simulations can give valuable insight into the process taking place at the mineral–water interface. For the siliceous zeolite LTA, we have found that the structuring of water is highly ordered, which in turn has a significant effect on the diffusivity at the surface. The simulations also indicate that the α-cages of {1 0 0} slab are hydrophobic. The simulations using different pH solutions show that the diffusion coefficient grows with increasing pH. The simulations also offer insight into the ordering of hydronium and Cl^- ions at the surface, thereby having an influence to water orientation and diffusivity data. The scope of this continued project is very broad and includes the consideration of surface charge, the inclusion of aluminum in the zeolite structure, different LTA surface terminations, as well as the adsorption of surface adsorbates, such as TCDD.

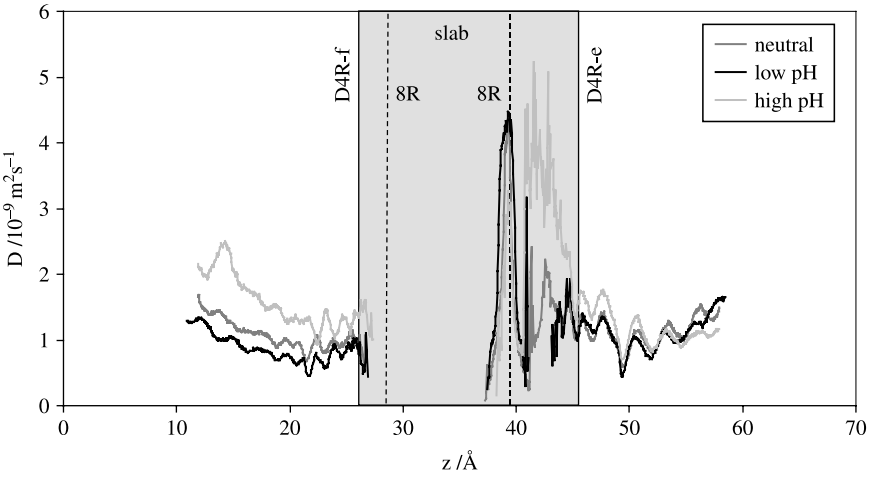

Figure 18. Diffusion coefficients D_z of water perpendicular to the surface for a {1 0 0} slab of siliceous LTA at three different pH levels.

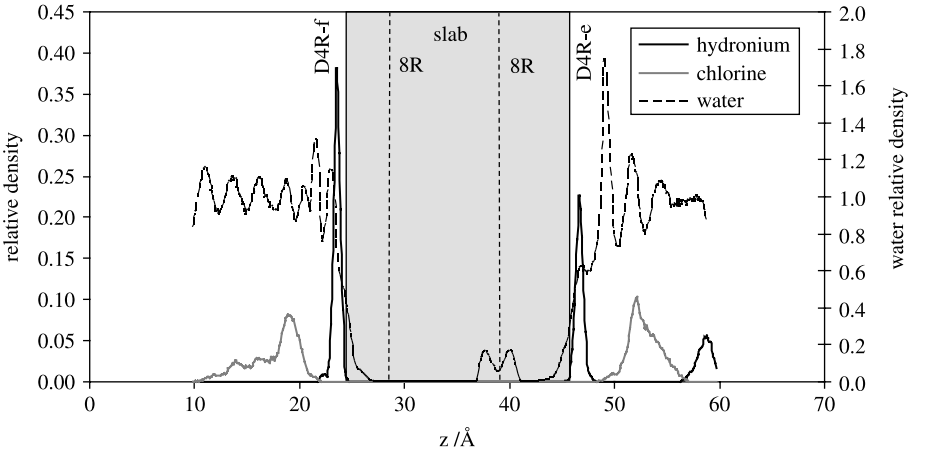

Figure 19. Plot showing the relative densities of H_3O^+ and Cl^- ions to the surfaces of {1 0 0} slab of siliceous LTA in low pH conditions. The relative density of water in the *z*-direction is also included for reference.

5. Conclusions

We have shown a number of current examples where we use static or dynamical simulations based on shell model interatomic potentials to study oxide and mineral interfaces. Firstly, static simulation techniques on gadolinium-doped ceria grain boundaries, represent an efficient tool for scanning different configurations to find the most stable structures and the segregation energies of defects as a function of distance from the interface, not least because the simulations are so quick that the configuration can be fully minimised at each step. The results of the stability of three ceria twin grain boundaries suggest that the twin (3 1 1) boundary is the most stable, due to the close matching and regularity seen at the interface. The higher energy (3 1 0) surface produces the least stable boundaries however, because the rearrangement of the cerium and oxygen sublattices causes a large degree of mismatch. Our results also indicate that the gadolinium and oxygen vacancy segregation will depend on the structure of the interface, with the enthalpies of segregation converging to zero at a much deeper distance into the bulk for gadolinium than that for the oxygen vacancy. This suggests that there is a larger number of available regular sites for the replacement with a trivalent dopant rather than the oxygen vacancy.

The method of scanning a large number of different configurations was then extended to consider the adsorption of carbonate at the mineral–vacuum interface on the low energy surfaces of magnesium and calcium hydroxide. The study reveals that magnesium hydroxide has poor reactivity directly with carbonate adsorption, which is in

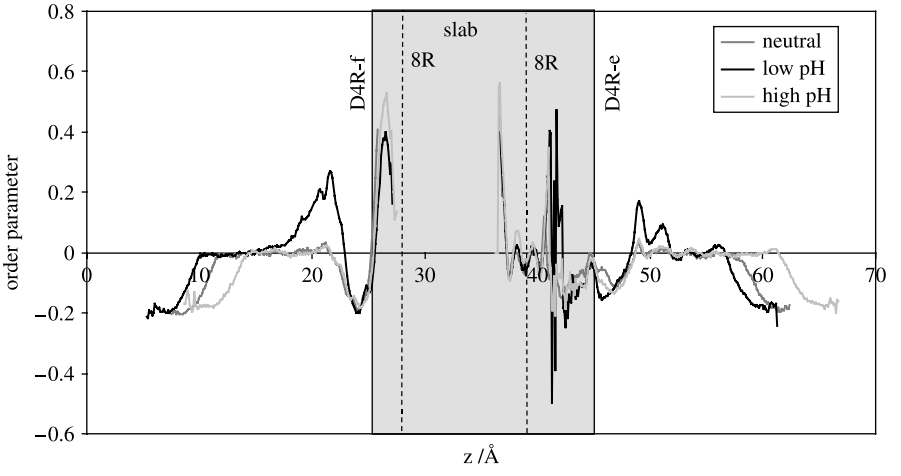

Figure 20. The orientation order parameter of water, as a function of the *z*-coordinate of the cell, around a {1 0 0} slab of siliceous LTA for three different pH solutions of water.

agreement with studies highlighting the requirement of a dehydroxylation step prior to carbonate adsorption. However, {1 0 1} and {2 0 1} surfaces of calcium hydroxide do show some stabilisation due to carbonate adsorption, and in particular would compete favourably on the surface to the gas phase adsorption of water.

Dynamical models were then used to probe the mineral–water interface, enabling the investigation of the interface structure and the effect of surface alteration and solution pH. The results from the study of the CaO surfaces indicated that above the pure surfaces there is clearly defined water layering occurring which is directly influenced by the surface structure. Flat surfaces with a regular arrangement of atoms, for example {1 0 0} and terraces between steps on {3 1 0} surface result in the formation of flat layers of highly mobile water at a distance of about 2.4 Å above the surface, which extend into the surface by four to five layers. However, rougher surfaces, such as {1 1 1} surface and the step edges of {310} surface, give rise to localised regions of more strongly coordinated water, which would particularly affect surface diffusion and adsorption. Surface carbonation resulted in a clear disruption and reduction of water layering, with the formation of mainly localised regions of water rather than distinct layers, which extended into the bulk to a reduced extent.

The structure of water was then considered in two differing silica environments. The first to be considered was the low index surfaces of α-quartz where we also considered the effect of the structuring of water on the adsorption of the hydrophobic TCDD. Results indicate that {10.0} quartz surface is more hydrophilic than the {11.0} due to the arrangement of surface hydroxyl groups. This is seen to result in a more highly ordered structure of water above {10.0} surface with faster diffusion. The adsorption of the dioxin is seen to be much more favourable on the hydrophobic surface in a wet environment. Silica also has the ability to form highly porous structures in the form of zeolites. This porous nature can significantly affect both the interaction with water as well as the diffusivity at the surfaces, which is of a particular interest due to their porous nature. The results showed the formation of highly ordered water structures on the D4R-terminated surfaces of LTA. This layering is seen to significantly influence the diffusion properties in the direction perpendicular to the surface, with the value of D_z seen to oscillate in a similar manner to the density of the water. At extreme pH levels the diffusion and water structures do change, particularly at low pH where hydronium ions segregate to the surface, compensated by a diffuse layer of Cl^-. This layering causes a greater influence on the orientation of water molecules at the surface in comparison to that seen for neutral and high pH conditions.

In summary, the work detailed in this study provides further evidence of the effectiveness of computer simulation to consider the adsorption and segregation processes which can occur at mineral oxide interfaces. In addition, it also emphasises the usefulness of atomistic simulation techniques for studying these processes when there are large numbers of either different configurations or atoms in the simulation cell.

Acknowledgements

We would like to thank EPSRC (Grant Number EP/D053897/2), AWE, and a NERC thematic programme for funding the various projects detailed in this work. In addition, acknowledgment is given to D.W. Price and M. S. D. Read (AWE), A. Benge for initial work on the carbonation of hydroxide surface and U. Anselmi-Tamburini for useful and informative discussions relating to the ceria grain boundaries. The eMinerals project, which is part of eScience, is also acknowledged along with the following members of the Nanogrowth consortium: M. Anderson, B. Slater and D.W. Lewis.

Computer resources used for the calculations above include those provided by the MOTT2 facility (EPSRC Grant GR/S84415/01) run by the STFC e-Science Centre.

References

[1] M. Born and K. Huang, *Dynamical Theory of Crystal Lattices*, Oxford University Press, Oxford, 1954.
[2] D.E. Parry, *The electrostatic potential in the surface region of an ionic crystal*, Surf. Sci. 49 (1975), pp. 433–440.
[3] D.E. Parry, *Erratum*, Surf. Sci. 54 (1976), p. 195.
[4] P.P. Ewald, *Die berechnung optischer und elektrostatischer gitterpotentiale*, Ann. Phys. 64 (1921), pp. 253–287.
[5] B.G. Dick and A.W. Overhauser, *Theory of dielectric constants of alkali halide crystals*, Phys. Rev. 112 (1958), pp. 90–103.
[6] G.W. Watson, E.T. Kelsey, N.H. de Leeuw, D.J. Harris, and S.C. Parker, *Atomistic simulations of dislocations, surfaces and interfaces in MgO*, J. Chem. Soc., Faraday Trans. 92 (1996), pp. 433–438.
[7] W. Smith and T.R. Forester, *DL_POLY_2.0: a general-purpose parallel molecular dynamics simulation package*, J. Mol. Graph. 14 (1996), pp. 136–141.
[8] S. Nosé, *A unified formulation of the constant temperature molecular dynamics methods*, J. Chem. Phys. 81 (1984), pp. 511–519.
[9] W.G. Hoover, *Canonical dynamics – equilibrium phase-space distributions*, Phys. Rev. A 31 (1985), pp. 1695–1697.
[10] L. Verlet, *Computer 'experiments' on classical fluids. I. Thermodynamical properties of Lennard-Jones molecules*, Phys. Rev. 159 (1967), pp. 98–103.
[11] P.J. Mitchell and D. Fincham, *Shell-model simulations by adiabatic dynamics*, J. Phys. Condens. Mater 5 (1993), pp. 1031–1038.
[12] B.C.H. Steele, *Appraisal of $Ce_{1-y}Gd_yO_{2-y/2}$ electrolytes for IT-SOFC operation at 500°C*, Solid State Ionics 129 (2000), pp. 95–110.
[13] H. Inaba and H. Tagawa, *Ceria based solid electrolytes*, Solid State Ionics 83 (1996), pp. 1–16.
[14] M. Mogensen, N.M. Sammes, and G.A. Tompsett, *Physical, chemical and electrochemical properties of pure and doped ceria*, Solid State Ionics 129 (2000), pp. 63–94.
[15] V.V. Kharton, F.M.B. Marques, and A. Atkinson, *Transport properties of solid oxide electrolyte ceramics a brief review*, Solid State Ionics 174 (2004), pp. 135–149.
[16] C. Xia, Y. Lang, and G. Meng, *Recent advances to the development of low-temperature solid oxide fuel cells*, Fuel Cells 4 (2004), pp. 41–47.
[17] B.C.H. Steele and A. Heinzel, *Materials for fuel-cell technologies*, Nature 414 (2001), pp. 345–352.
[18] R.A. De Souza, M.J. Pietrowski, U. Anselmi-Tamburini, S. Kim, Z.A. Munir, and M. Martin, *Oxygen diffusion in nanocrystalline yttria-stabilized zirconia: the effect of grain boundaries*, Phys. Chem. Chem. Phys. 10 (2008), pp. 2067–2072.

[19] U. Anselmi-Tamburini, F. Maglia, G. Chiodelli, A. Tacca, G. Spinolo, P. Riello, S. Bucella, and Z.A. Munir, *Nanoscale effects on the ionic conductivity of highly doped bulk nanometric cerium oxide*, Adv. Funct. Mater. 16 (2006), pp. 2363–2368.
[20] Y. Lei, Y. Ito, N.D. Browing, and T.J. Mazanec, *Segregation effects at grain boundaries in fluorite-structured ceramics*, J. Am. Chem. Soc. 85 (2002), pp. 2359–2363.
[21] S. Kim, J. Fleig, and J. Maier, *Space charge conduction: simple analytical solutions for ionic and mixed conductors and application to nanocrystalline ceria*, Phys. Chem. Chem. Phys. 5 (2003), pp. 2268–2273.
[22] J. Maier, *Nanoionics: ion transport and electrochemical storage in confined systems*, Nat. Mater. 4 (2005), pp. 805–815.
[23] X. Guo and R. Waser, *Electrical properties of the grain boundaries of oxygen ion conductors: acceptor-doped zirconia and ceria*, Prog. Mater. Sci. 51 (2006), pp. 151–210.
[24] L. Minervini, M.O. Zacate, and R.W. Grimes, *Defect cluster formation in M_2O_3-doped CeO_2*, Solid State Ionics 116 (1999), pp. 339–349.
[25] G. Balducci, M.S. Islam, H. Kašpar, P. Fornasiero, and M. Graziani, *Bulk reduction and oxygen migration in the ceria-based oxides*, Chem. Mater. 12 (2000), pp. 677–681.
[26] M. Nolan, S.C. Parker, and G.W. Watson, *The electronic structure of oxygen vacancy defects at the low index surfaces of ceria*, Surf. Sci. 595 (2005), pp. 223–232.
[27] T.X.T. Sayle, S.C. Parker, and C.R.A. Catlow, *Surface segregation of metal ions in cerium dioxide*, J. Phys. Chem. 98 (1994), pp. 13625–13630.
[28] C.A.J. Fisher and H. Matsubara, *Molecular dynamics investigations of grain boundary phenomena in cubic zirconia*, Comput. Mater. Sci. 14 (1999), pp. 177–184.
[29] T.X.T. Sayle, S.C. Parker, and D.C. Sayle, *Shape of CeO_2 nanoparticles using amorphisation and recrystallisation*, Chem. Commun. 21 (2004), pp. 2438–2439.
[30] P. Martin, D. Spagnoli, A. Marmier, S.C. Parker, D.C. Sayle, and G.W. Watson, *Application of molecular dynamics DL_POLY codes to interfaces of inorganic materials*, Mol. Simul. 32 (2006), pp. 1079–1093.
[31] G. Balducci, J. Kašpar, P. Fornasiero, M. Graziani, M.S. Islam, and J.D. Gale, *Computer simulation studies of bulk reduction and oxygen migration in CeO_2–ZrO_2 solid solutions*, J. Phys. Chem. B 101 (1997), pp. 1750–1753.
[32] P. Martin, S.C. Parker, D.C. Sayle, and G.W. Watson, *Atomistic modeling of multilayered ceria nanotubes*, Nano Lett. 7 (2007), pp. 543–546.
[33] W. Seifritz, *CO_2 disposal by means of silicates*, Nature 345 (1990), p. 486.
[34] H. Béarat, M.J. McKelvy, A.V.G. Chizmeysha, R. Sharma, and R.W. Carpenter, *Magnesium hydroxide dehydroxylation/carbonation reaction processes: implications for carbon dioxide mineral sequestration*, J. Am. Ceram. Soc. 85 (2002), pp. 742–748.
[35] N.H. de Leeuw, G.W. Watson, and S.C. Parker, *Atomistic simulation of the effect of dissociative adsorption of water on the surface structure and stability of calcium and magnesium oxide*, J. Phys. Chem. 99 (1995), pp. 17219–17225.
[36] S. Kerisit, S.C. Parker, and J.H. Harding, *Atomistic simulation of the dissociative adsorption of water on calcite surfaces*, J. Phys. Chem. B 107 (2003), pp. 7676–7682.
[37] S.V. Churakov, M. Iannuzzi, and M. Parrinello, Ab initio *study of dehydroxylation-carbonation reaction on brucite surface*, J. Phys. Chem. B 108 (2004), pp. 11567–11574.
[38] N.H. de Leeuw, F.M. Higgins, and S.C. Parker, *Modelling the structure and stability of α-quartz*, J. Phys. Chem. B 103 (1999), pp. 1270–1277.
[39] P.S. Baram and S.C. Parker, *Atomistic simulation of hydroxide ions in inorganic solids*, Philos. Mag. B 73 (1996), pp. 49–58.
[40] S. Kerisit, D.J. Cooke, A. Marmier, and S.C. Parker, *Atomistic simulation of charged iron oxyhydroxide surfaces in contact with aqueous solution*, Chem. Commun. 24 (2005), pp. 3027–3029.
[41] A. Pavese, M. Catti, S.C. Parker, and S. Wall, *Modelling of the thermal dependence of structural and elastic properties of calcite, $CaCO_3$*, Phys. Chem. Miner. 23 (1996), pp. 89–93.
[42] N.H. de Leeuw and S.C. Parker, *Molecular-dynamics simulation of MgO surfaces in liquid water using a shell-model potential for water*, Phys. Rev. B 58 (1998), pp. 13901–13908.
[43] G.V. Lewis and C.R.A. Catlow, *Potential models for ionic oxides*, J. Phys. C: Solid State Phys. 18 (1985), pp. 1149–1161.
[44] E. Stockelmann and R. Hentschke, *A molecular-dynamics simulation study of NaCl(100) using a polarizable water model*, J. Chem. Phys. 110 (1999), pp. 12097–12107.
[45] R.W. Impey, P.A. Madden, and I.R. McDonald, *Hydration and mobility of ions in solution*, J. Phys. Chem. 87 (1983), pp. 5071–5083.
[46] M. Van der Berg, L.S. Birnbaum, L.S. Denison, M. De Vito, W. Farland, M. Feeley, H. Fiedler, H. Hakansson, A. Hanberg, L. Haws, et al., *The 2005 World health organisation reevaluation of human and mammalian toxic equivalency factors for dioxin and dioxin-like compounds*, Toxicol. Sci. 93 (2006), pp. 223–241.
[47] M.J. Sanders, M. Leslie, and C.R.A. Catlow, *Interatomic potentials for SiO_2*, J. Chem. Soc. Chem. Commun. 19 (1984), pp. 1271–1273.
[48] S. Kerisit and S.C. Parker, *Free energy of adsorption of water and metal ions on the {1014} calcite surface*, J. Am. Chem. Soc. 126 (2004), pp. 10152–10161.
[49] K. de Boer, A.P.J. Jansen, R.A. van Santen, G.W. Watson, and S.C. Parker, *Free-energy calculations of thermodynamic, vibrational, elastic, and structural properties of α-quartz at variable pressures and temperatures*, Phys. Rev. B 54 (1996), pp. 826–835.
[50] W. Steurer, A. Apfolter, M. Koch, W.E. Ernst, B. Holst, E. Sondergard, and S.C. Parker, *Low-energy surface phonons on α-quartz (0001)*, Phys. Rev. B 78 (2008), 035402-1-035402-5.
[51] S.L. Mayo, B.D. Olafson, and W.A. Goddard, *Dreiding – a generic force-field for molecular simulations*, J. Phys. Chem. 94 (1990), pp. 8897–8909.
[52] P. Dauberosguthorpe, V.A. Roberts, D.J. Osguthorpe, J. Wolff, M. Genest, and A.T. Hagler, *Structure and energetics of ligand-binding to proteins* – Escherichia coli *dihydrofolate reductase trimethoprim, a drug-receptor system*, Proteins 4 (1988), pp. 31–47.
[53] W.A. Deer, R.A. Howie, and J. Zussman, *An Introduction to the Rock-Forming Minerals*, Longman Scientific & Technical, New York, 1992.
[54] B. Fubini, V. Bolis, A. Cavenago, E. Garrone, and P. Ugliengo, *Structural and induced heterogeneity at the surface of some SiO_2 polymorphs from the enthalpy of adsorption of various molecules*, Langmuir 9 (1993), pp. 2712–2720.
[55] L. Marple, R. Brunck, and L. Throop, *Water solubility of 2,3,7,8-tetrachlorodibenzo*-para-*dioxin*, Environ. Sci. Technol. 20 (1986), pp. 180–182.
[56] W. Meier, D. Olson, and C. Baerlocher, *Atlas of Zeolite Structure Types*, Elsevier, London, 1996.
[57] B. Slater, J.O. Titiloye, F.M. Higgins, and S.C. Parker, *Atomistic simulation of zeolite surfaces*, Curr. Opin. Solid State Mater. Sci. 5 (2001), pp. 417–424.
[58] R.A. Jackson and C.R.A. Catlow, *Computer simulation studies of zeolite structure*, Mol. Sim. 1 (1988), pp. 207–224.
[59] P. Tschaufeser and S.C. Parker, *Thermal expansion behaviour of zeolites and $AlPO_4$s*, J. Phys. Chem. 99 (1995), pp. 10609–10615.
[60] F.M. Higgins, N.H. de Leeuw, and S.C. Parker, *Modelling the effect of water on cation exchange in zeolite A*, J. Mater. Chem. 12 (2001), pp. 124–131.
[61] S. Sugiyama, S. Yamamoto, O. Matsuoka, H. Nozoye, J. Yu, G. Zhu, S. Qiu, and O. Terasaki, *AFM observation of double 4-rings on zeolite LTA crystals surface*, Micropor. Mesopor. Mater. 28 (1999), pp. 1–7.
[62] T. Wakihara, Y. Sasaki, H. Kato, Y. Ikuharac, and T. Okubo, *Investigation of the surface structure of zeolite A*, Phys. Chem. Chem. Phys. 7 (2005), pp. 3416–3418.
[63] D. Spagnoli, D.J. Cooke, S. Kerisit, and S.C. Parker, *Molecular dynamics simulations of the interactions between the surfaces of polar solids and aqueous solutions*, J. Mater. Chem. 16 (2006), pp. 1997–2006.
[64] S.J. Marrink and H.J.C. Berendsen, *Simulation of water transport through a lipid-membrane*, J. Phys. Chem. 98 (1994), pp. 4155–4168.